North Carolina Agricultural and Technical State University
Aggie Digital Collections and Scholarship

Theses | Electronic Theses and Dissertations

2013

Dynamics Of Water In Aircraft Fuel Tanks During Flight Maneuvers

Shiraz Zahid Moughal
North Carolina Agricultural and Technical State University

Follow this and additional works at: https://digital.library.ncat.edu/theses

Recommended Citation

Moughal, Shiraz Zahid, "Dynamics Of Water In Aircraft Fuel Tanks During Flight Maneuvers" (2013). *Theses*. 290.
https://digital.library.ncat.edu/theses/290

This Thesis is brought to you for free and open access by the Electronic Theses and Dissertations at Aggie Digital Collections and Scholarship. It has been accepted for inclusion in Theses by an authorized administrator of Aggie Digital Collections and Scholarship. For more information, please contact iyanna@ncat.edu.

Dynamics of Water in Aircraft Fuel Tanks during Flight Maneuvers

Shiraz Zahid Moughal

North Carolina A&T State University

A thesis submitted to the graduate faculty

in partial fulfillment of the requirements for the degree of

MASTER OF SCIENCE

Department: Mechanical Engineering

Major: Mechanical Engineering

Major Professor: Dr. John P. Kizito

Greensboro, North Carolina

2013

School of Graduate Studies
North Carolina Agricultural and Technical State University
This is to certify that the Master's Thesis of

Shiraz Zahid Moughal

has met the thesis requirements of
North Carolina Agricultural and Technical State University

Greensboro, North Carolina
2013

Approved by:

Dr. John P. Kizito Major Professor	Dr. Gary Tatterson Committee Member
Dr. Cynthia K. Waters Committee Member	Dr. Samuel Owusu-Ofori Department Chair

Dr. Sanjiv Sarin
Dean, The Graduate School

© Copyright by

Shiraz Zahid Moughal

2013

Biographical Sketch

Shiraz Zahid Moughal was born in Faisalabad, Pakistan. He attended high school in Jeddah, Saudi Arabia. Shiraz Zahid Moughal received his Bachelor of Science degree in Mechanical Engineering from North Carolina Agricultural and Technical State University in 2008. Shiraz Zahid Moughal is a candidate for the Masters of Science in Mechanical Engineering from North Carolina Agricultural and Technical State University.

Dedication

I dedicate my work to my wife, and parents.

Acknowledgements

I would like the thank NASA URC funding Grant # NNX09AV08A finding, and North Carolina Space Grant for supporting this research. In addition, I would like to thank Dr. John P. Kizito for many uncountable things.

Table of Contents

Abstract 1

CHAPTER 1 Introduction 2

1.1 Specific Objectives 2

1.2 Impact 3

CHAPTER 2 Literature Review 4

2.1 Background 4

2.2 Nucleation of Water in Immiscible Liquids 8

2.3 Solubility of Water in Jet Fuel or Kerosene 13

2.4 Measurement of Interfacial Properties of Water in Jet Fuel 15

2.4.1 Contact angle. 15

2.4.2 Surface and interfacial tension. 17

CHAPTER 3 Methods and Material 25

3.1 Understanding the Behavior of Water and Jet Fuel in a Fuel Tank 25

3.1.1 Hardware assembly. 25

3.1.2 The construction of the fuel tank assembly. 26

3.2 Measurement of Volume Fraction of Water in Kerosene 29

3.3 Determination of the Tank Tilt Angle Relative to the Gravitational Vector 30

3.4 Calculation of Pressure Difference Due To the Pump 33

3.5 Calculation of G-Force Exerted On the Fuel Tank While Banking 34

3.6 Determination of Roll Frequency 36

3.7 Calculations for Liquid–Liquid Pressure and Velocity in Fuel Tank 37

3.8 Setup of Computational Simulation 39

3.8.1 Inlet and outlet conditions. 40

3.8.2 Body forces on the tank. 40

3.8.3 Sloshing of the fuel tank 41

3.8.4 Initial and boundary conditions. 41

3.9 The Grid Independence Study 41

3.10 Contact Angle and Interfacial Tension Measurements 43

3.10.1 Surface tension. 43

3.10.2 Contact angle. 47

3.10.3 Hardware assembly for interfacial tension measurement. 48

3.11 Measuring Contact Angle and Interfacial Tension by Image Processing 51

3.12 Experimental Uncertainties 55

CHAPTER 4 Results 56

4.1 Contact Angle and Interfacial Tension of Water and Kerosene 56

4.2 Experimental Simulation Results 57

4.2.1 Aircraft during taking-off and landing mode. 57

4.2.2 Aircraft banking turns. 58

4.3 Simulation of Fuel-Water Dynamics in a Tank Subjected To External Forces 61

4.3.1 Simulation of fuel tank while aircraft is banking left. 61

4.3.2 Simulation of fuel tank while aircraft is banking right. 63

4.3.3 Fuel tank while in oscillation motion..... 64

CHAPTER 5 Concluding Remarks and Future Research..... 66

References..... 68

List of Figures

Figure 1. (a) The crash site at London Heathrow (Winter, 2010). (b) The formation of ice inside the heat exchanger (Haines, 2008). 5

Figure 2. Illustration of fuel system of Cessna 172N (Cessna, 1978). 5

Figure 3. (a) Fuel tank vent of the piper 128-181. (b) Chart of Temperature vs. The wind speed (NOAA, 2001). 6

Figure 4. The schematics of Cessna 182 fuel tank taken from the SRM. 7

Figure 5. Sequence of images of pure water droplets in Jet A-1 fuel as they were cooled at the rate of 10° C/minute (B. Murray, et al., 2011). 9

Figure 6. Fraction of droplets containing known concentrations of kaolinite versus the temperature range (B. J. Murray, et al., 2011). 10

Figure 7. (a) List of refineries from where the carbohydrates were obtained. (b) Effect of temperature on the solubility of water in carbohydrates (Aldrich, 1931). 14

Figure 8. (a) Plot of relative transparency of jet fuel versus fuel temperature. (b) Water nucleation on a flat sub-cooled aluminum surface as the jet fuel was cooled (Lao, et al., 2011). 15

Figure 9. The contact angle indicates the wettability of a liquid. 16

Figure 10. The effect of temperature on contact angle of water droplets on aluminum (Bernardin, et al., 1997). 16

Figure 11. Temperature versus the contact angle of water in isopropyl alcohol (Iordan, 2000). 17

Figure 12. Measurement of interfacial tension by using Du Noüy Ring method (Noüy, 1925). 18

Figure 13. The illustration of the micrometer and liquid cell arranged for Du Noüy-Padday method (Christian, et al., 1998). 18

Figure 14. Illustrates the contact angle being measured using the Wilhelmy plat method (David & Kin, 1999). 19

Figure 15. Balance of static pressure in bubble pressure method (Fainerman, et al., 1994). 20

Figure 16. Plot of the correction factor, F, with respect to $rV1/3$ of water (D. X. Du, et al., 2012). 21

Figure 17. The Capillary rise method used to measure surface tension (Sheng-Shan & Xin, 2011). 22

Figure 18. Measuring of surface tension using the pendant drop method (Arashiro & Demarquette, 1999)..... 23

Figure 19. Boiling ranges of Jet fuel and kerosene are highlighted in the boxes (Institute, 2010). 25

Figure 20. An illustration of the experimental setup for the fuel tank. 26

Figure 21. Photograph of the test rig. 27

Figure 22. (a) The red dyed kerosene dominates clear water in the image. (b) The image converted into 8-bit for image analysis. 29

Figure 23. (a) Clear kerosene and green dyed water used for the experiments. (b) Converted the RBG image into 8-bit for analysis. (c) Outline of the 8-bit image after analysis. 30

Figure 24. Climb chart for the PA-28-181. 31

Figure 25. Descend chart for the PA-28-181. 32

Figure 26. Free body diagram of an aircraft while banking. 35

Figure 27. Free body diagram of an aircraft fuel tank in a roll. 37

Figure 28. An illustration of fuel tank at an inclination having water and kerosene. 38

Figure 29. An experimental illustration of computer-simulated fuel tank. 40

Figure 30. Snapshot of the elements used for grid independence study. 43

Figure 31. Comparison of simulations at time 2.5 seconds using different grid sizes. 43

Figure 32. A two dimensional illustration of liquid drop on top of a solid surface. 44

Figure 33. A free body diagram of the surface tension of the droplet 45

Figure 34. Force balance at three-component contact angle..... 47

Figure 35. An illustration of the experimental setup to measure contact angle and interfacial tension of water droplet in various liquids. 49

Figure 36. An illustration of the fabricated container. 51

Figure 37. (a) Contact angle of water droplet on acrylic surrounded by air. (b) Contact angle of water droplet on acrylic surrounded by kerosene. 53

Figure 38. (a) Contact angle of water droplet on aluminum surrounded by air. (b) Contact angle of water droplet on aluminum surrounded by kerosene. 53

Figure 39. 8-bit images of water droplets for the measurement contact angles. 54

Figure 40. (a) Measurement of the interfacial tension of water in air. (b) Measurement of the interfacial tension of water in kerosene. 54

Figure 41. The water residue amounts in the fuel tank as a function of the tank inclination angle during aircraft banking mode. 58

Figure 42. Time taken by water to clear the fuel line port area versus the fuel tank angle of inclination during banking. 59

Figure 43. (a) Top view of water (colored green) in dispersed in kerosene (less than 5º). (b) Top view of water (greater than 5º)..... 60

Figure 44. At the entrance of fuel line water domain pinning down towards the bottom of the fuel tank. 61

Figure 45. The dynamics of water due to gravitational forces caused by a left turn. 62

Figure 46. The volume fraction of water while turning left. 62

Figure 47. The dynamics of water due to gravitational forces caused by a right turn. 63

Figure 48. The volume fraction of kerosene while airplane turning right. 64

Figure 49. The dynamics of water caused oscillation motion of an airplane. 65

Figure 50. The volume fraction of kerosene during the airplane is in an oscillatory roll motion.

..... 65

List of Tables

Table 1. Comparison of different methods used to determine the Surface/Interface tension (Dukhin, Kretzschmar, & Miller, 1995; Schramm, 2000; Xu, 2005). 24

Table 2. List of components used for the construction of the fuel tank. 26

Table 3. Parameters used to find the angle while taking off. 32

Table 4. Calculations for finding the angle of decent 33

Table 5. Parameters used in calculating pressure 34

Table 6. List of the values used in calculating the maximum G-Force. 36

Table 7. List of the physical parameters of the liquid used in the simulation. 39

Table 8. Values of different constants for the gravitational vectors. 41

Table 9. List of boundary conditions used in the computer simulation. 41

Table 10. Volume covered by the kerosene with respect to the number of elements. 42

Table 11. List of components used in the experiment to measure the contact angle. 48

Table 12. Contact angle measurements of water droplet in the air and kerosene. 56

Table 13. Interfacial tension measurements of water droplet in various liquids. 57

Table 14. Average residence time and volume of water in tank during taking off and landing ... 58

Abstract

The goal of the current research is to study the dynamics of water in fuel tanks during flight maneuvers. The study was motivated by the fact that airplane fuel tanks can be exposed to extremely low temperatures, whereby water can nucleate and freeze, in turn causing the fuel lines to clog. Therefore, ice formation in the fuel system may lead to aviation safety issues. Different scenarios were considered which influence the movement of water and kerosene in a fuel tank. A test rig was constructed to replicate airplane motions when taking off, landing, and turning. Computer-simulated experiments were performed to replicate airplane motions under roll maneuvers and when turning right or left. The computer model required the a priori knowledge of interfacial properties of water in kerosene. These properties were experimentally measured and were used as input data for the computer simulation. The surface tension of water was confirmed as 72.9 mN/m, and the surface tension of water in kerosene (the interfacial tension between kerosene and water) was measured as 6.78 mN/m. The contact angle of water in kerosene on aluminum and plexiglass was measured as 114.9º and 121.1º, respectively. The contact angle of water in the air on aluminum and plexiglass was measured to be 49.6º and 64.6º, respectively. The experimental simulations showed that water took 114.9 seconds to clear the fuel line port while the tank was in a takeoff mode, compared to 121.8 seconds while the tank was in landing mode. The time taken for water to clear the fuel line decreased before it increased when the tank inclination was changed from 0 to 30º. In addition, the volume of water remaining in the fuel tank decreased as the tilt angle was increased. The computer-simulated experiments were performed for an airplane undergoing right and left banking motion in addition to roll motions. The results showed that the resultant acceleration vector and magnitude had a significant influence on the local composition and movement of water in the fuel tank.

CHAPTER 1

Introduction

The goal of the present study is to understand the formation of ice inside the fuel tank. Water can nucleate in the fuel handling system of an aircraft. Ice formation in the fuel system may lead to fatal crashes if not properly addressed. Ice related accidents are increasing in number because of an increase in the numbers of airplane traffic. There has not been much research done on the ice buildup inside the fuel system of the aircraft although there has been a lot of research done on ice formation on aircraft surfaces (Cao & Chen, 2010; Y. X. Du, Gui, Xiao, & Yi, 2010; Fortin, Mayer, & Perron, 2008; Huttunen-Saarivirta, Kuokkala, Kokkonen, & Paajanen, 2009; Ratvasky, Barnhart, & Lee, 2010; Yanxia, Yewei, Chunhua, & Xian, 2010). In the literature review, presented in Chapter 2, shows that there are few papers on the effect of temperature on water inside the fuel tank (Lao, Ramshaw, Yeung, & Carpenter, 2011; Benjamin J. Murray, Broadley, & Morris, 2011). In the literature review, none of the papers described the dynamics of water in the fuel tank while the aircraft is under acceleration. Safe operation of an airplane requires the knowledge of water-fuel dynamics in the fuel handling system under operational flight conditions. Following are specific objectives formulated to meet the research goal for the thesis.

1.1 Specific Objectives

The present thesis will addressed the following two objectives:

1. To measure the interfacial properties of water in kerosene, in particular, surface tension or interfacial tension and contact angle.
2. To analyze the parameter that affect fuel-water dynamics in a fuel tank at varying tilt angles under simulated airplane maneuvers:

a. to determine the profile of water/kerosene interface
b. to determine the time taken by water to clear the fuel-line exit port region under the same conditions

1.2 Impact

The knowledge of interfacial tension number is required in numerical simulation of the water and kerosene. Understanding how water behaves in a fuel system will drastically affect the design of the fuel tanks in the future. Design improvements may deter ice formation in fuel lines, which will improve in aviation safety. The thesis is organized as following: In Chapter 2 the literature review is presented. The methods and materials are discussed in Chapter 3. The results are discussed in Chapter 4. Lastly in Chapter 5, the conclusion is given.

CHAPTER 2

Literature Review

2.1 Background

Ice in the fuel tank is a problem for all aircrafts. Compared to larger commercial aircraft smaller aircraft are much more vulnerable to icing (Rutherford, 2001). Usually in large commuter airplanes, the fuel pump is immersed in the fuel. The fuel pump produces enough heat to raise the temperature of the fuel tank above 0° C so that the water in the fuel tanks will not freeze (Andrade & Tenning, 1992). The results can be devastating for both large and small aircrafts if the fuel pump is malfunctioning. The London Heathrow 2008 incident, a Boeing aircraft, 777-236 ER, lost power in its engines. British Airways Flight 38 crashed just short of the runway and injured 47 people. The cause was determined to be ice crystals clogging the fuel-oil heat exchanger, FOHE, of both engines (U.K., 2010).

Figure 1a shows the destroyed BA Boeing 777-236 ER at London Heathrow. Figure 1b shows the ice formation inside the FOHE that was considered the cause of the crash. A similar incident happened when one of the engines of Delta Airlines Flight 18 lost power at 39,000 feet (Croft, 2008). The Delta Airlines Flight 18 landed safely, but the cause of the engine stall was also determined to be crystals forming at the FOHE.

Compared to larger aircrafts, smaller aircrafts are even more likely to fail due to icing (Isaac et al., 2001). FAA does not allow small aircrafts to operate in storms (Lanicci et al., 2012). The fuel tanks of small passenger aircrafts are not pressurized therefore, pressure outside and inside of the fuel tank is same. Most small commuter aircrafts are designed with vents. Figure 2 illustrates the fuel system of a Cessna Skyhawk Model 172 N private aircraft that has an open vent. Air is continuously entering the fuel tank from the vent and the filler cap.

(a)

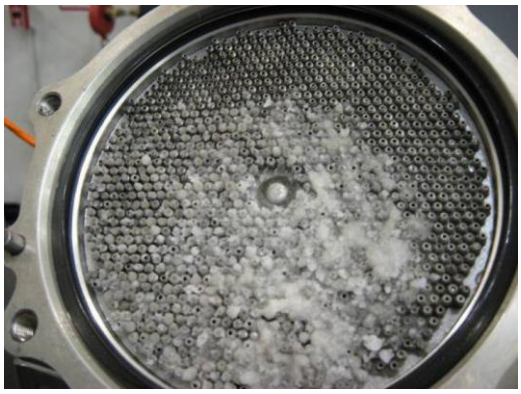

(b)

Figure 1. (a) The crash site at London Heathrow (Winter, 2010). (b) The formation of ice inside the heat exchanger (Haines, 2008).

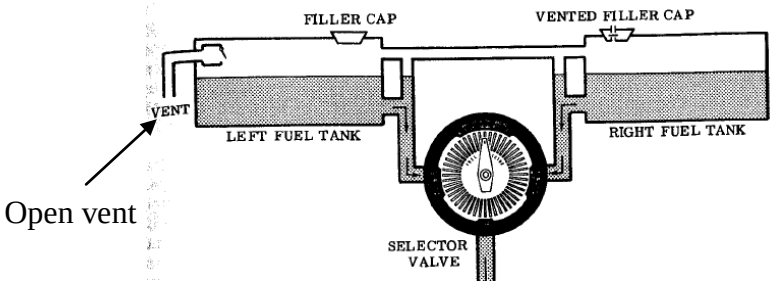

Figure 2. Illustration of fuel system of Cessna 172N (Cessna, 1978).

The overflow line outside of the tank can be seen in Figure 3a, which also serve as vents. The Figure 3a is the fuel tank of the Piper 128-181. The vents facilitates the air to enter the tank (Cessna, 1978). Sometimes these drains are connected to both fuel tanks, located on each side. The drains are used to keep the fuel tank from over flowing and to keep pressure inside and outside of the tank similar. The fuel tanks are usually attached inside a wing of the aircraft, if the pressure in not similar the shape of the wing may buckle and result in wing loosing lift. The atmosphere has moisture, which in time of flight may accumulate into water sitting at the bottom of the fuel tank.

The FAA requires pilots to drain water from the fuel tanks before every flight (MacDonald, 2011). Unpressurized fuel tanks are common among small commuter aircrafts. The overflow line is subject to the atmosphere. The overflow line can result in accumulation of high humidity in the fuel tank which over time will turn into the water in the tank on a high humidity day (Nevins, Rohles, Springer, & Feyerherm, 1966). The operation speed of the Piper 128-181 is 125 Knots which is equal to 231.5 km/h and the operating altitude is 12,000 ft which is equal to 3657.6 m (Tulapurkara, Ananth, & Kulkarni, 2007). The temperature of atmosphere at 3657.6 m is -8.76º C (Lewis, 1947). The resulting temperature on the aircraft surface due to wind chill will be even lower (NOAA, 2001). Figure 3b displays the wind chill table used by the National Oceanic and Atmospheric Agency.

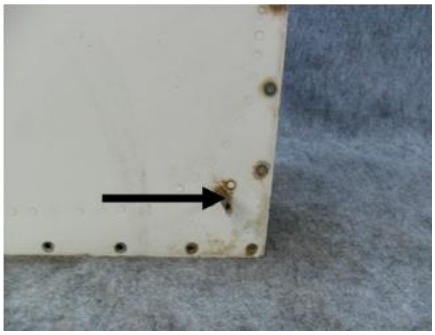

(a)

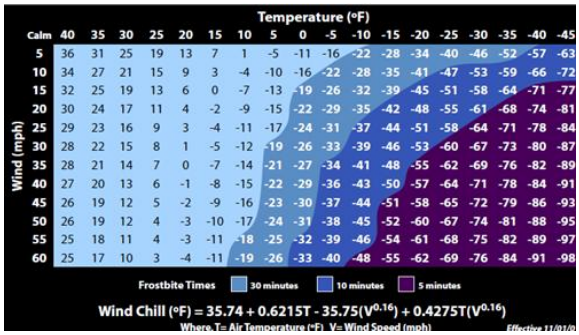

(b)

Figure 3. (a) Fuel tank vent of the piper 128-181. (b) Chart of Temperature vs. The wind speed (NOAA, 2001).

The wind chill temperature depends on the temperature of the air and the velocity of the wind, which can be calculated by Equation 2.1.

$$T_{WC} = 13.12 + 0.6215\,T_{air} - (11.37 - 0.3965\,T_{air})V^{0.16} \quad (2.1)$$

In Equation 2.1, T_{WC} is the temperature due to wind chill in °C, T_{air} is the temperature of air in °C and V is the velocity of the air in km/h (Shitzer & De Dear, 2006).

The connection of the fuel line to the fuel tank can be observed in Figure 4. The Figure 4 is the schematics of Cessna 182 fuel tank taken from the Standard Reference Manual, SRM. The Figure 4 shows that the fuel line is located at the bottom of the tank. The information helped in the decision of connecting the fuel line to the fuel tank that is discussed later in Chapter 3.

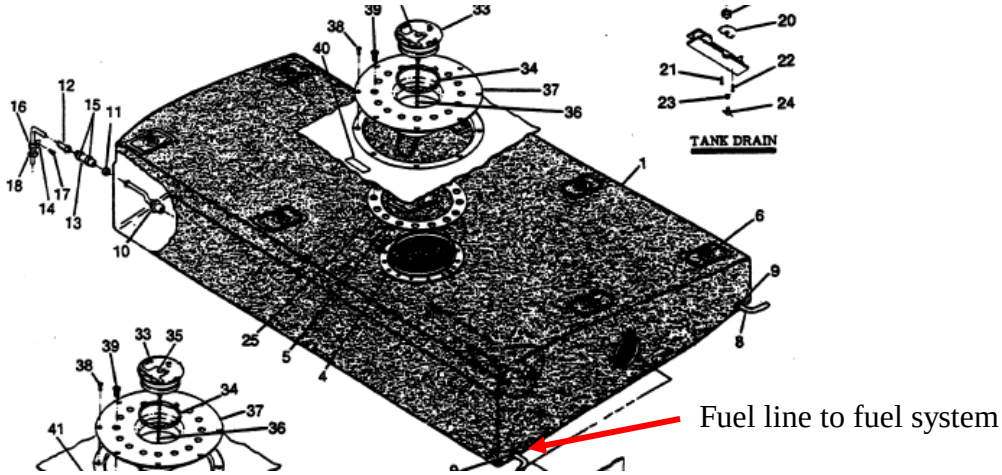

Figure 4. The schematics of Cessna 182 fuel tank taken from the SRM.

The following points from the fuel tank studies were establish. The fuel tank is not pressurized due to the vents and the filler cap. Water in the fuel tank accumulates due to moisture in the atmosphere. The fuel line is connected to the fuel tank on the bottom side of the tank.

2.2 Nucleation of Water in Immiscible Liquids

As discussed earlier, the clogging of airliner's FOHE is due to the nucleation of water in the fuel system. The clogging of FOHE leaded to determine the behavior of water in fuel at sub-low temperatures, and determining the conditions, that lead water changes its phase when submerged in an immiscible liquid. The nucleation of fluid happens in two forms: homogeneous and heterogeneous nucleation. Homogeneous nucleation happens when a fluid changes its phase without contacting any surface (Abraham & Zettlemoyer, 1974). Hetrogeneous nucleation occurs when a fluid changes its phase as it comes in contact with another surface (Vali, 1971).

Micron size water droplets immersed in Jet A-1 fuel can exist in a meta-stable sub-cooled state to a temperature of -36° C (B. Murray, Broadley, Wilson, Atkinson, & Wills, 2011). The majority of the droplets in their investigation froze homogeneously, showing that the fuel itself did not facilitate in the crystallization of water droplets in ice formation. The study suggested that water particles would remain in a sub-cooled liquid state until the water particles encounter a suitable solid surface. The experiment was performed using filtered water droplets in the micron size range that were briefly produced using a homemade nebulizer and deposited onto a hydrophobic glass coating onto a glass. The hydrophobic coating was used on the glass so that the glass surface does not act as a nucleation point. The study discovered that the nucleation had a direct relationship with droplet size. Water droplets in the micron size range could be sub-cooled to -36° C when immersed in jet-fuel. Figure 5 shows water droplets submerged in jet-fuel at different temperatures. The Figure 5 also shows that water droplets remained liquid at -30.9º C, while the water droplets are fully frozen at -39º C.

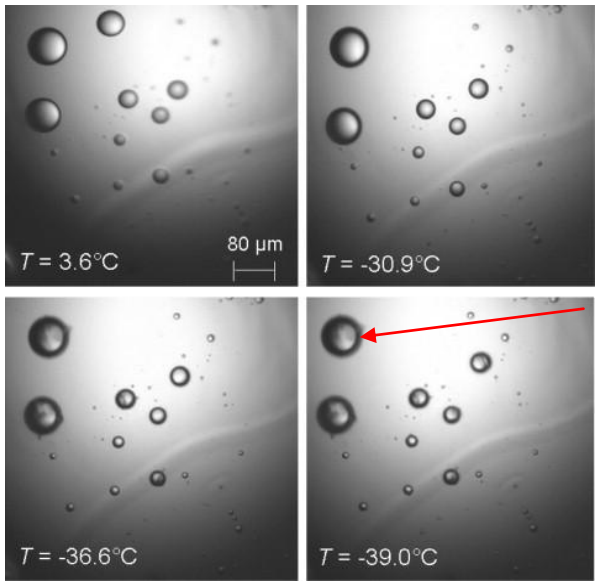

Figure 5. Sequence of images of pure water droplets in Jet A-1 fuel as they were cooled at the rate of 10° C/minute (B. Murray, et al., 2011).

The number of the ice formation is in direct correlation with the number of nucleation points (B. J. Murray, et al., 2011). Figure 6 shows the relationship between formations of ice particles with respect to the amount of clay introduced. The cloud formation was controlled by the amount of clay, dust particles, introduced in the experiment. The dust particles acted as a nucleation point for water. The number of frozen droplets depends on the lowering the temperature during cooling and depends on keeping constant temperature, as a function of time. Both ice particles and super cooled liquid water droplets coexisted at temperatures lower than -37.15° C. The mixture of water and clay was cooled at a rate ranging between 0.8 to 10 K/minute. The water droplets decreased exponentially as they froze over time under constant temperature.

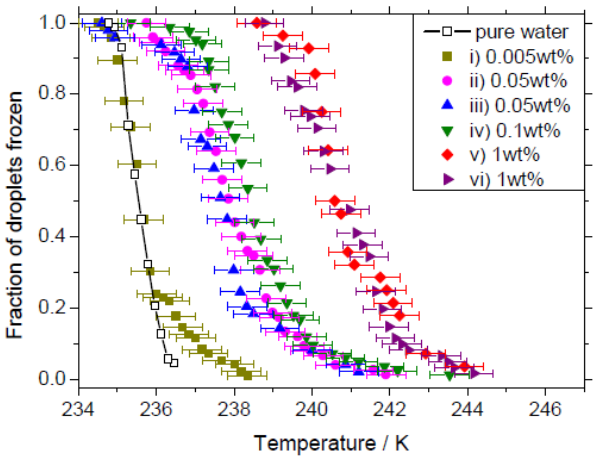

Figure 6. Fraction of droplets containing known concentrations of kaolinite versus the temperature range (B. J. Murray, et al., 2011).

Emulsions can be produced with a wide range of droplet sizes. Large bodies of water inside petroleum jelly can be held in super-cooled temperature below -36° C for four days without freezing (Taborek, 1985). The calorimetric method was used to determine the nucleation rate of ice of super cooled H_2O, and D_2O droplets in petroleum jelly. The nucleation-rate and the mixture of H_2O and D_2O with petroleum jelly are determined by monitoring the release of heat from fusion as the droplets froze. The emulsions were prepared by dissolving 0.1 to 0.01 g of sorbitan tristearate (STS) as a surfactant in 5 g of melted petroleum jelly. The water and heavy water were both passed through 0.2 micrometer filter. The mixture had 10% water by volume. The mean droplet diameter was 6 micrometers. The size of the resulting water droplets are affected by the surface tension between liquids and petroleum jelly, the amount of the petroleum jelly mixture, and the temperature of petroleum jelly.

Droplets of the same size remain unfrozen at a constant temperature, which leads to volume variations of droplet sizes (Wood & Walton, 1970). The nucleation-rates of ice from water droplets were calculated by observing the frequencies at which water droplets solidified.

An emulsion of oil and water was used for the experiment. The nucleation rate was calculated by measuring the frequency of droplets solidification. The size of water the droplets ranged from 2 to 50 microns. The droplets were categorized with respect of their diameters in the experiment. Observations made from the study are, nucleation rate of water droplets depended on the volume of the droplets, the emulsion temperature, and experimental pressure. Temperature kept on fluctuating, even though it was set to be constant, due to nucleation of water droplets.

Crystalline structure of water depends on the temperature at which the water crystallizes (B.J. Murray & Bertram, 2005). Studies were done on the formulation of cubic shape ice of water droplets suspended in oil in relation to the droplet size. The results show that the droplets of 5.6 microns froze into cubic shape ice, and it shows hexagonal shape ice formation for the water droplets from 5.6 to 17.0 microns. For the experiment, a mixture of water and oil was prepared with water 30 to 40% in oil by mass. Crystalline phase was cubic when water droplets were frozen homogeneously at -38.15º C. The transformation of cube ice to hexagonal ice is time and temperature dependent. The proceedings from cubic ice to hexagonal ice went rapidly at first, and then the transformation slowed down, and then stopped indefinitely. Hexagonal shape is the final stage of the ice crystals.

Viscosity and yields stress of water oil emulsion depends on the amount of water in the emulsion (Rensing, Liberatore, Sum, Koh, & Dendy Sloan, 2011). The study is on the formation of ice in water-in-crude oil emulsion in various volume fractions of fresh water and brine. Brine is the mixture of NaCl and water. The yield stress of the liquid emulsion appears to increase as the fraction of water increases. No shear stress was observed at 0.25 of water by volume. The shear stress at about 300 Pascal was observed from 0.25 to 0.55 of water by volume. Ice particles caused the rheometer to jam when 0.55 of water by volume was used. Emulsions were

cooled to -10° C, and the viscosity and yield stress were analyzed as a function of time after nucleation.

The phenomena associated with ice accretion on the surface depends on the liquid runback of water along the ice surface (Naterer, 2011). The thickness of the ice depends on the liquid water run and on the surface energy input by the boundary at the boundary layer on which the ice is being formed. A time dependent model is studies to predict the ice growth along the curved heated surface. The curved surface could serve as a nucleation point for water at low temperature. The experiment was performed on a heated cable subjected to the sub-cooled water droplets. The model showed an agreement between ice-growth significantly as the heat input is lowered.

The ice will grow mostly on a surface that has many nucleation points, provided that the surface temperature is kept at a sub-cool fixed temperature (Myers & Hammond, 1999). The experiment was preceded at -10° C. Water droplets freeze suddenly the moment they run into with sub-cooled surface temperature. The following analysis can be made from this study. The thickness of ice is directly proportional to the temperature differences of the surface and the freezing temperature. The coefficient of conduction through water will decrease with a decrease in the source of incoming fluid, an increase in the surface temperature, or increase in the sink temperature that is the temperature of water. The growth rate of glaze ice depends on an increase of the coefficient for conduction through ice, which is directly proportional to the temperature difference of the final surface, and a decrease in the coefficient of conduction when there is any liquid water present. The growth rate of glaze ice also depends on an increase in the water layer thickness since the water conduction coefficient is greater than zero, and the heat transfer coefficient at the surface can lead to the initial ice growth.

The following conclusion can be made from the nucleation of water; water droplets will not change phase until they find a nucleation point. The nucleation rate depends on the size of the droplets. The temperature drops exponentially once the phase change is complete. The nucleation rate depends on the temperature difference and exposure time. Nucleation rate depends on the volume of the droplets and the temperature rate. The physical structure of crystal water droplet after nucleation depends on the size of the droplet.

2.3 Solubility of Water in Jet Fuel or Kerosene

A possibility for water in the aviation fuel is due to the solubility of water in jet fuel (Englin, Plate, Tugolukov, & Pryanishnikova, 1965). Jet fuel is a natural observant of water. The solubility of water in aviation fuel is affected by change in temperate and pressure.

The solubility of water in fuel depends on the refinery from which fuel came (Aldrich, 1931). Aldrich performed the experiment by adding water into gasoline obtained from different refineries. Figure 7a shows the list of refineries from where the carbohydrates were acquired. The solubility of water decreases as the temperature decreases as illustrated in Figure 7b. The solubility of water in different carbohydrates ranged from 0.0036 to 0.0128% weight.

As the temperature decreases the solubility of water in hydrocarbon also decreases (Black, Joris, & Taylor, 1948). The authors studied solubility of water in hydrocarbons in their experiments. The experiments were performed at a minimum temperature of 5° C. The study showed that solubility of water in fuel depends on the temperature.

Oil and water when left in contact for a longer period of time will occur coalesce (Ata, Pugh, & Jameson, 2011). The study was conducted by placing two drops of kerosene in a tank of water. The temperature of the experiment ranged from 22 to 75° C. The coalescence of kerosene droplets in water also increased as the temperature increased, and there was no

coalescence as the temperature increased from 65 to 75° C. The experiment was performed using two different types of kerosene. The first type of kerosene had a slight blue color; it was classified as a technical grade product (KT-1), with a flashpoint of 38° C, and boiling point between 145 and 300° C. The second type of kerosene was colorless, it was classified as analytical grade kerosene, had a flash point of 70° C, and a higher boiling point between 190 and 250° C. Coalescence occurred in both hydrocarbons used in the experiment.

Fuel	Source
10	Oklahoma natural gasoline
12	West Virginia natural gasoline
13	California crude
15	Midcontinent crude
19	Oklahoma natural gasoline

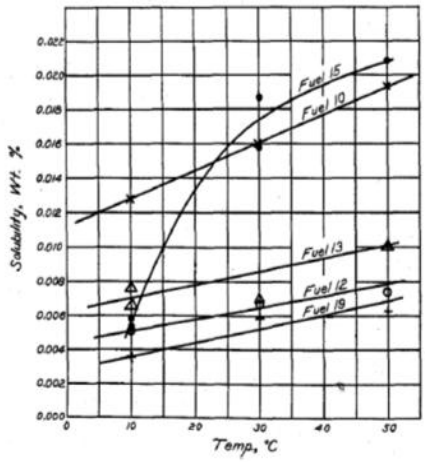

(a) (b)

Figure 7. (a) List of refineries from where the carbohydrates were obtained. (b) Effect of temperature on the solubility of water in carbohydrates (Aldrich, 1931).

The icing of the water crystals were observed in an investigation when jet fuel was cooled to sub-low temperatures (Lao, et al., 2011). Fog phenomenon was observed in the fuel tank when the temperature started lowering. The fog was due to the nucleation of water at a sub-cooled temperature. Shown in Figure 8a is the plot of relative clarity of fuel with respect to temperature. The transparency of the fuel decreased as the temperature decreased. The solubility of water in jet fuel decreases at lower temperatures. The crystallization of water at the bottom of the tank was observed as the temperature of the fuel tank was lowered even further.

The crystallization of water droplets is shown in Figure 8b. Ice crystals were seen at the bottom of the tank at temperatures below -10º C.

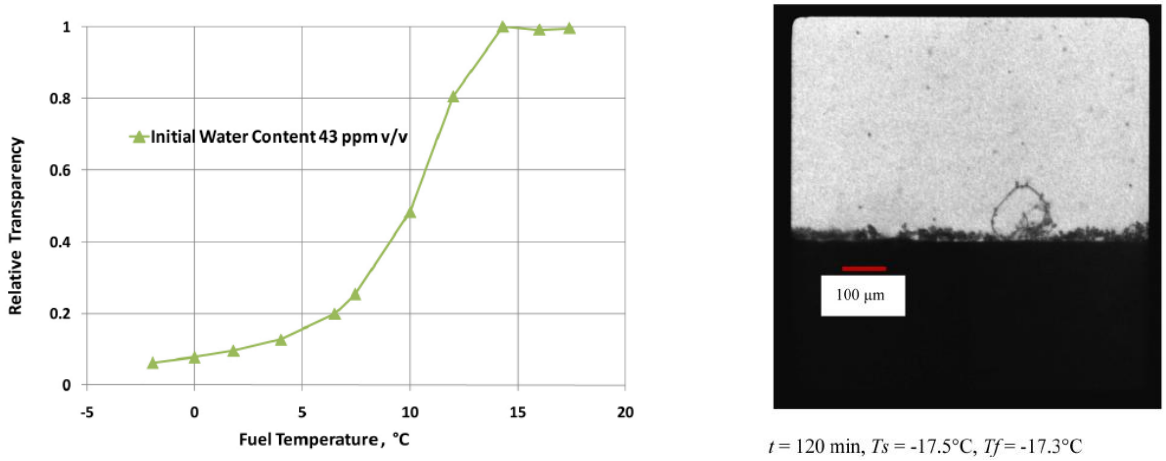

(a) (b)

Figure 8. (a) Plot of relative transparency of jet fuel versus fuel temperature. (b) Water nucleation on a flat sub-cooled aluminum surface as the jet fuel was cooled (Lao, et al., 2011).

The following points are from the water in jet fuel: As the temperature decreases, the solubility of water also decreases. Coalescence increases as the temperature increases. The transparency of the Jet fuel decreases as the temperature decreases.

2.4 Measurement of Interfacial Properties of Water in Jet Fuel

2.4.1 Contact angle. The contact angle is the angle which a liquid/vapor or liquid/liquid interface meet a solid surface (Mittal, 2009). The contact angle quantifies the wettability of a solid surface by a liquid. A drop of the liquid will spread on the solid if the contact angle is small called spreading. The drop will bead up when the angle is large. The surface is called non-wetting. Figure 9 illustrates that the substrate is wet by the liquid if the contact angle $\theta < 90°$, the surface non-wetting if $\theta > 90°$.

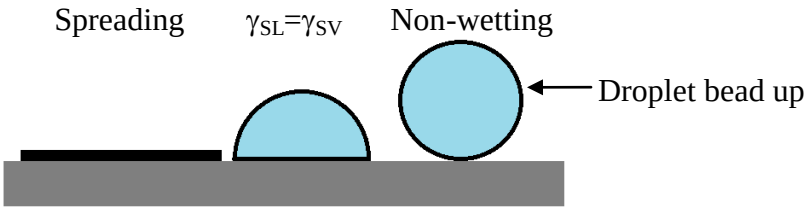

Figure 9. The contact angle indicates the wettability of a liquid.

The contact angle of water on aluminum depends on the temperature and the pressure of the surroundings (Bernardin, Mudawar, Walsh, & Franses, 1997). The study was conducted by coating an aluminum surface with different materials. Different amounts of pressure and temperature were used to determine their impact on the contact angle. The amounts of temperatures were ranging from 25 to 170º C, and the pressures ranging from 101.3 to 827.4 kPa in their experiment. The contact angle was 90º at temperatures below 120º C, and contact angle decreased in a linear manner when the temperatures were above 120º C. Figure 10 shows the effect of temperature on the contact angle of droplets when the aluminum was coated with different materials.

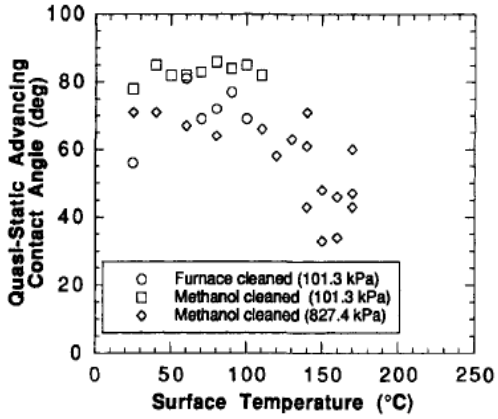

Figure 10. The effect of temperature on contact angle of water droplets on aluminum (Bernardin, et al., 1997).

The change from the wetting state to the non-wetting state is the result of the temperature influencing the characteristics of the liquid (Iordan, 2000). A change in the contact angle was observed for isopropyl alcohol at 12º C. The temperature is below the critical temperature of isopropyl. Figure 11 shows the effect of temperature on the contact angle.

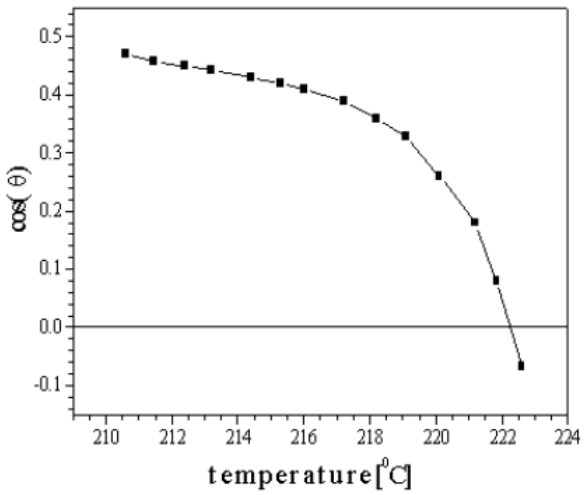

Figure 11. Temperature versus the contact angle of water in isopropyl alcohol (Iordan, 2000).

2.4.2 Surface and interfacial tension. Interfacial tension is the property of a liquid to allow a liquid to resist an external force due to internal molecular forces (Saad, Policova, & Neumann, 2011). These strong intermolecular forces between the molecules of the free surface are called *surface tension*, and if there is an immiscible liquid as a substitute of gas, then this free surface is called *interfacial tension* (Hartland, 2004).

There are different ways to measure the interfacial tension. The methods are listed in the following: the Du Noüy Ring method (Lunkenheimer & Wantke, 1978), the Du Noüy-Padday method (Christian, Slagle, Tucker, & Scamehorn, 1998; Padday, Pitt, & Pashley, 1975) the Wilhelmy plate method, the Spinning drop method, the Pendant drop method, the Bubble pressure method, the Drop volume method, and the Capillary rise method (David & Kin, 1999).

The Du Noüy Ring Method: The method uses a platinum ring that is lifted slowly from the liquid surface. The force required to raise the ring from the liquid's surface is measured. The measured force can be related to the surface tension (Noüy, 1925). Figure 12 describe the measuring of interfacial tension of water and carbon tetra chloride.

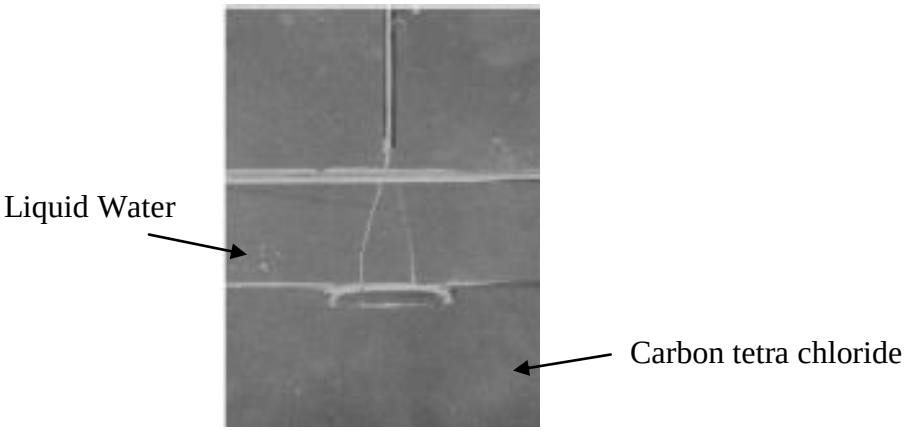

Figure 12. Measurement of interfacial tension by using Du Noüy Ring method (Noüy, 1925).

The Du Noüy-Padday Method: Instead of a ring, a metal rod is used to determine the surface tension. The liquid is placed in a container. The force required to raise the rod out of the container is related to the surface tension of the liquid as illustrated in Figure 13 (Christian, et al., 1998).

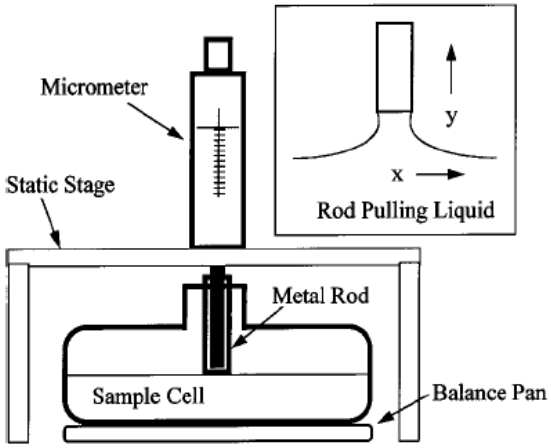

Figure 13. The illustration of the micrometer and liquid cell arranged for Du Noüy-Padday method (Christian, et al., 1998).

The Wilhelmy Plate Method: A plate made of either platinum or glass is used (David & Kin, 1999). When the bottom of a vertically hanging plate comes in to contact with the liquid's surface, the liquid makes an upward meniscus while wetting the plate. This method determines the surface tension by measuring the force pushing the plate downward, using a counter balance. Figure 14 illustrates the contact angle using the Wilhelmy plate method. The surface tension is measured by using the Equation 2.2.

$$\gamma = \frac{F}{Dcos\theta_0} \tag{2.2}$$

In Equation 2.2, *D* is the depth of the plate inside the liquid, θ_0 is the angle of the meniscus, *F* is the force applied to keep the meniscus straight, and γ is the surface tension.

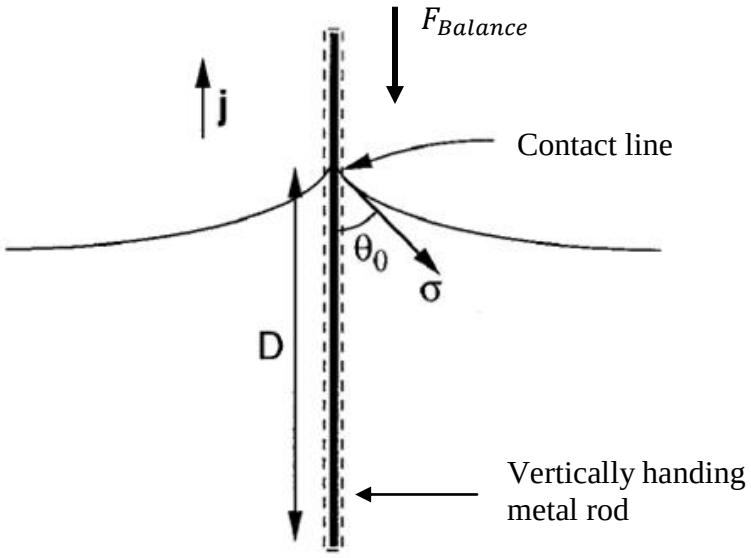

Figure 14. Illustrates the contact angle being measured using the Wilhelmy plat method (David & Kin, 1999).

The Spinning Drop Method: The spinning drop method is commonly used for measuring extremely low interfacial tensions (Viades-Trejo & Gracia-Fadrique, 2007; Vonnegut, 1942). A drop of liquid 1 is placed inside liquid 2. Liquid 2 has a higher density than liquid 1. Both of the liquids are placed inside a clear tube. Then the tube is spun at 20,000 rpm, which results in the

elongating of the liquid 1 drop. Equation 2.3 is used to calculate the interfacial tension by using the spinning drop method.

$$\gamma = \frac{\omega^2 \Delta\rho r^2}{A} \tag{2.3}$$

In Equation 2.3, ω is the rotational speed, ΔP is the pressure difference between liquid 1 and liquid 2, r is the radius of the curvature of the droplet, and A is surface area of the plate.

The Bubble Pressure Method: A bubble is blown at the tip of a tube which is dipped into a liquid (Fainerman, Miller, & Joos, 1994). The bubble grows inside the liquid as the pressure increases. The radius of the curvature of the bubble at the interface decreases at first, reaches a minimum, and then increases as illustrated in Figure 15. Equation 2.4 is the equation used to calculate the surface tension in bubble pressure method.

$$\gamma = \frac{\rho g(h_2 - h_1)R}{2} \tag{2.4}$$

In Equation 2.2, h_1 and h_2 are the height of the liquid, ρ is the density of the fluid, and R is the radius of the bubble at maximum radii shown in Figure 15.

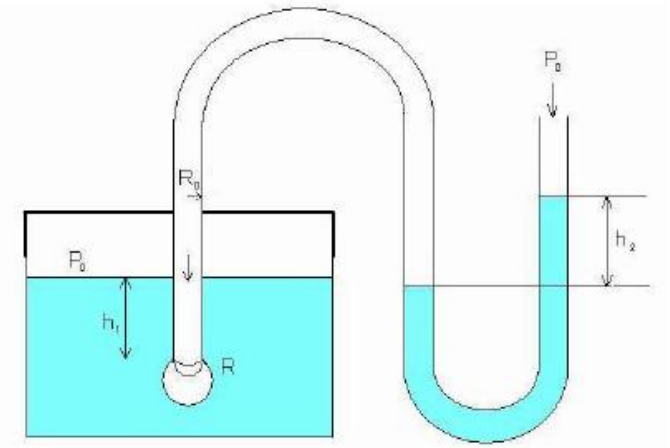

Figure 15. Balance of static pressure in bubble pressure method (Fainerman, et al., 1994).

The Drop Volume Method: The drop volume method is used by measuring the radius of the droplet forming at the tip of a vertical tube (D. X. Du, Geng, Sun, & Li, 2012). Equation 2.5 shows the force balance of the drop at the edge of the tube.

$$2\pi r\sigma = mg. \tag{2.5}$$

Equation 2.5 is simplified by substituting the weight of the droplet which is defined a function of $\frac{r}{V^{\frac{1}{3}}}$, where *r* is the radius of the droplet, and *V* is the volume. Hence, the Equation 2.5 yield to

$$\gamma = \frac{mg}{2\pi r}F \tag{2.6}$$

where $F = \frac{r}{v^{\frac{1}{3}}}$. *F* is the correction factor, *r* is the radius of the droplet, and *v* is the volume of droplet in Equation 2.6. Figure 16 shows the relationship between $F = \frac{r}{v^{\frac{1}{3}}}$, and $\frac{r}{v^{\frac{1}{3}}}$. Figure 16 shows the relationship between correction factors with respect to $\frac{r}{v^{\frac{1}{3}}}$.

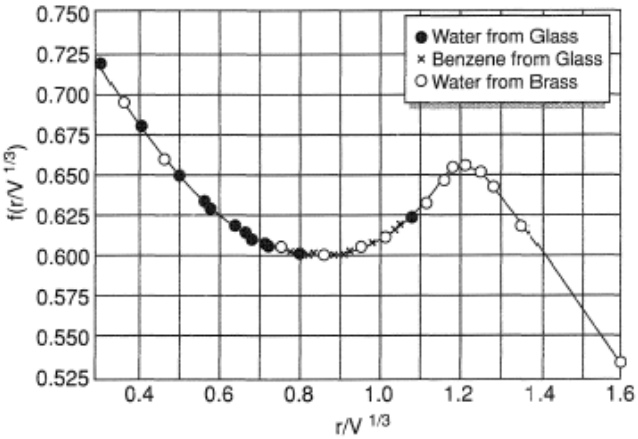

Figure 16. Plot of the correction factor, *F*, with respect to $\frac{r}{V^{1/3}}$ of water (D. X. Du, et al., 2012).

The Capillary Rise Method: Capillary phenomena occur due to the pressure difference across curved meniscus of the liquid rise and base of the liquid (Sheng-Shan & Xin, 2011). A tube is dipped into a pool of liquid, resulting the rise of that liquid. Figure 17 illustrates how the

Capillary rise method is used to determine the surface tension of a liquid. Equation 2.7 is used to measure surface tension.

$$\gamma = \frac{r}{2} h(\rho_L - \rho_V) g \tag{2.7}$$

In Equation 2.7, r is the radius of the tube, h is the height of the liquid, ρ_L is the density of the liquid, ρ_V is the density of the vapor, and g is gravity.

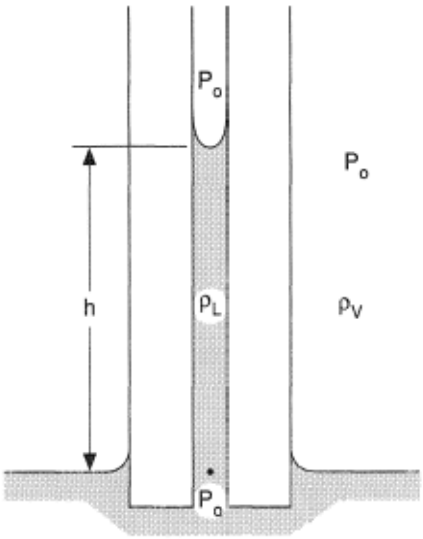

Figure 17. The Capillary rise method used to measure surface tension (Sheng-Shan & Xin, 2011).

Pendant Drop Method: A drop of liquid is suspended from a tube by surface tension (Arashiro & Demarquette, 1999; Saad, et al., 2011). The length of the boundary between the liquid and the tube is proportional to the surface tension. Hence, the force due to surface tension is given by

$$F_\gamma = \pi d \gamma. \tag{2.8}$$

where F_γ is the surface tension force, d is the diameter of the tube, and γ is the surface tension.

The pendent drop method is probably the most convenient and the most common method to determine the surface and interfacial tension. This process is involved in determining the

profiles of drops of one liquid suspended in another liquid at equilibrium. This equilibrium is determined by balancing the surface tension and gravity. Figure 18 illustrates the measuring of the principal radii and height for the calculation of surface tension. Equation 2.9 is used to determine the surface/interfacial tension.

$$\gamma = (\rho_1 - \rho_2)gh\left(\frac{1}{R_1} + \frac{1}{R_2}\right)^{-1} \tag{2.9}$$

In Equation 2.9, ρ_1 is the density of fluid 1, the droplet density, ρ_2 is the density of fluid 2, usually the surrounding fluid, g is the acceleration due to gravity, h is the length of the droplet, and R_1 and R_2 are the principal radii of the droplet.

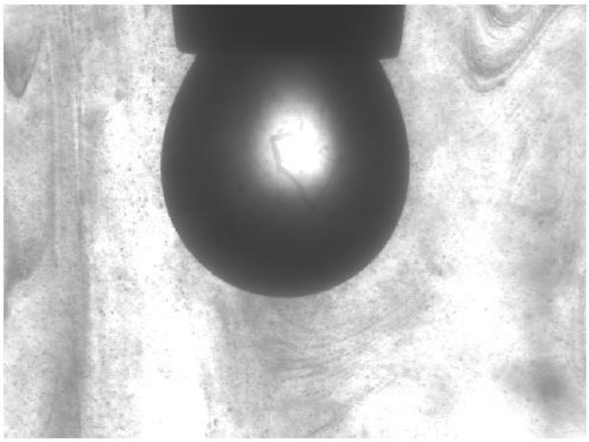

Figure 18. Measuring of surface tension using the pendant drop method (Arashiro & Demarquette, 1999).

Table 1 compares different techniques used to determine surface/interfacial tension. Table 1 also lists the accuracy of different techniques and its commercial availability. The surface tension of water in the air is 72.8 mN/m (Vargaftik, Volkov, & Voljak, 1983). Once the method to measure surface tension is chosen, the same approach can be used to determine the interfacial tension in between liquids. The pendent drop method was used because its ability of measuring the interfacial tension between two liquids and between gas and liquid surroundings.

Table 1.

Comparison of different methods used to determine the Surface/Interface tension (Dukhin, Kretzschmar, & Miller, 1995; Schramm, 2000; Xu, 2005).

Method	**Accuracy mN/m**	**Suitability**				**Time range**	**Commerical Avilable**
		Surfactant solutions	**Two-liquid systems**	**Gas-liquid**	**High Temperature and Pressure**		
Wilhelmy Plate	0.1	Limited	Good	Good	No	> 10 s	Yes
Du Nouy Ring	0.1	Limited	Reduced accuracy	Good	No	> 30 s	Yes
Maximum Bubble pressure	0.1 - 0.3	Very good	Very good	Good	No	1 ms - 100 s	Yes
Capillary Rise	< 0.1	Very good	Very good, Experimentally difficult	Good	No		No
Drop Volume	0.1 - 0.2	limited	Good	Good	Yes	1 s - 20 min	Yes
Pendent Drop	0.1	Very good	Very good	Good	Yes	10 s - 24 h	Yes
Sessile Drop	> 0.1	Good	Very good	Possible	Yes		No
Spinning Drop	0.0001	Good	Good (Small Range)	Possible	No		Yes

CHAPTER 3

Methods and Material

3.1 Understanding the Behavior of Water and Jet Fuel in a Fuel Tank

Kerosene was readily available and was used in the experiments instead of jet fuel since both have similar properties (Institute, 2010). The melting point of kerosene is -55° C while the melting point for jet fuel ranges from -50 to -47° C. The freezing point are either -40° C max for Jet A or -47° C max for JP-8 in The American Society for Testing and Materials (ASTM) and military specifications. There is no numerical number for the boiling point of jet fuel or kerosene. Fuels from different refineries boil at different temperatures as discussed in Chapter 2. Shown in Figure 19 are the boiling points of different fuels.

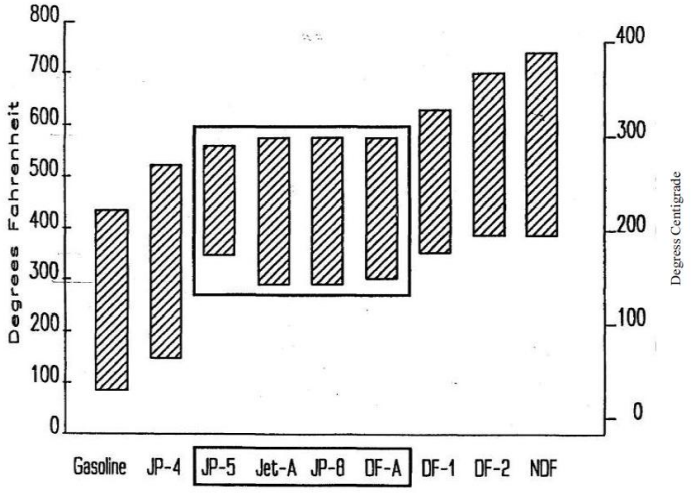

Figure 19. Boiling ranges of Jet fuel and kerosene are highlighted in the boxes (Institute, 2010).

3.1.1 Hardware assembly. To determine the dynamics of water in a fuel tank while an airplane is taking off, landing, or turning, an experimental rig was constructed to simulate extreme flight conditions. Figure 20 illustrates the experimental setup used to understand the behavior of water in a fuel tank. Figure 20 shows, (1) main tank made of Acrylic, (2) stand with

swivel joint that has 34° movement, (3) PA-128 fuel pump, (4) sight glass, (5) flow meter, and (6) holding tank. Table 2 is the list of parts used in the assembly of the test rig.

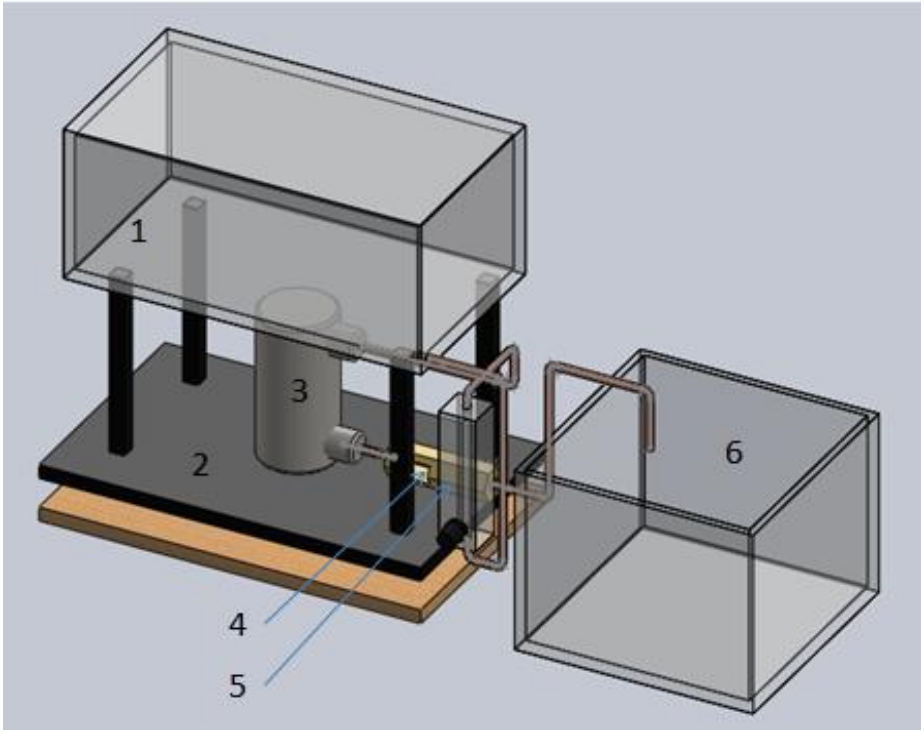

Figure 20. An illustration of the experimental setup for the fuel tank.

Table 2.

List of components used for the construction of the fuel tank.

#	Brand	Specification	Quantity
1	Generic	Clear Acrylic, 1/4 inch (0.635 cm) thick	1
2	Generic	Copper tube 50 feet	1
3	Generic	Plywood	1
4	Dwyer	Flow meter 0 – 12 GPH	1
5	Generic	Tripod	1
6	Liberty	Piper fuel pump	1
7	Generic	A Swivel joint	1
8	Mastech	Power supply HY1502D	1

3.1.2 The construction of the fuel tank assembly. A tank was constructed by from clear acrylic sheets. The size of the tank, shown in Figure 21 is 32 L × 15 W × 11.5 H cm.

Special attention was given to the sides of the tank so that a clear picture could be taken for analysis. The top of the tank was left open because the fuel tanks of small commuter aircrafts are not pressurized as explained in Chapter 2. Once the acrylic panels were cut to size, acrylic glue was used for the construction.

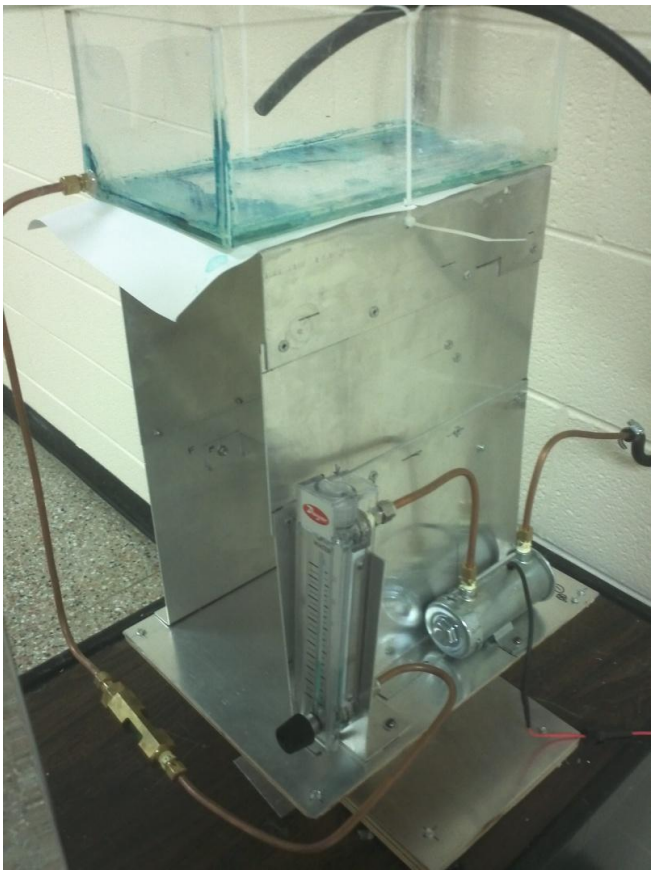

Figure 21. Photograph of the test rig.

Acrylic adhesive Weld-on # 3 by IPS Corporation was used for the construction of the tank. The adhesive has a clear finish, and once the adhesive is cured, joints cannot be adjusted. The adhesive took 2 to 5 minutes to hold and 24 to 48 hours for it to reach its full strength. A layer of sealant was applied to the edges of the tank to ensure that the fuel would not leak from the tank.

Kerosene resistant sealant called Seal-All manufactured by Eclectic Products, Inc. was used to ensure that there was not any leakage from the edges of the tank. The sealant took 30 minutes to 1 hour to cure. A sight glass was placed between the flow meter and the pump to view the profile of the liquid flow inside the tube. The housing of the glass was made of brass with female joints on the connector's sides.

A Dwyer flow meter was brought to measure the flow rate. The flow meter had a built in control valve, which was used to control the flow rate. The flow had to be between 2 to 3 GPH, which is the standard flight operation of a smaller commuter aircraft's fuel pump shown in the SRM of the PA-181. A fuel pump by, PMA Products, was bought for the experiment so that the actual conditions of the aircraft fuel tank can be simulated. The pump was made of stainless steel case. The fuel pump required 12 V of continuous power source.

A 12 V continuous power supply made by Mastech model # HY1502D was brought to power the pump. The voltage and amplitude could be controlled by the power supply.

As stated in Chapter 1, the scenarios chosen for the experiment were taking off, landing, and turning. A swivel joint was constructed using by the parts bought locally and attached to the bottom of the equipment. The swivel connection was made strong enough so that it could withstand the weight of all things on the platform. The swivel joint could reach angles of ± 30º. The material of the tube was not crucial since the goal of the research was to understand the fluid leaving the tank. Copper was picked because of the ease of the construction and the ease of availability.

Once the movies of different experimental runs were recorded, they were then analyzed. Special attention was paid to ensure that there was maximum contrast between the two liquids. Analyzing images becomes difficult when two liquids having low contrast between them.

3.2 Measurement of Volume Fraction of Water in Kerosene

Maximum contrast was achieved by using differently colored kerosene and water. K-1 red-dyed kerosene, which is easily obtainable from a gas station, was used first. Red color of kerosene dominated the images and the water was not visible at all as shown Figure 22. (a) The red dyed kerosene dominates clear water in the image. (b) The image converted into 8-bit for image analysis.Figure 22a. So when the images were analyzed in ImageJ, the image analysis software, the software picked up both areas of the liquid as one group as shown in Figure 22b.

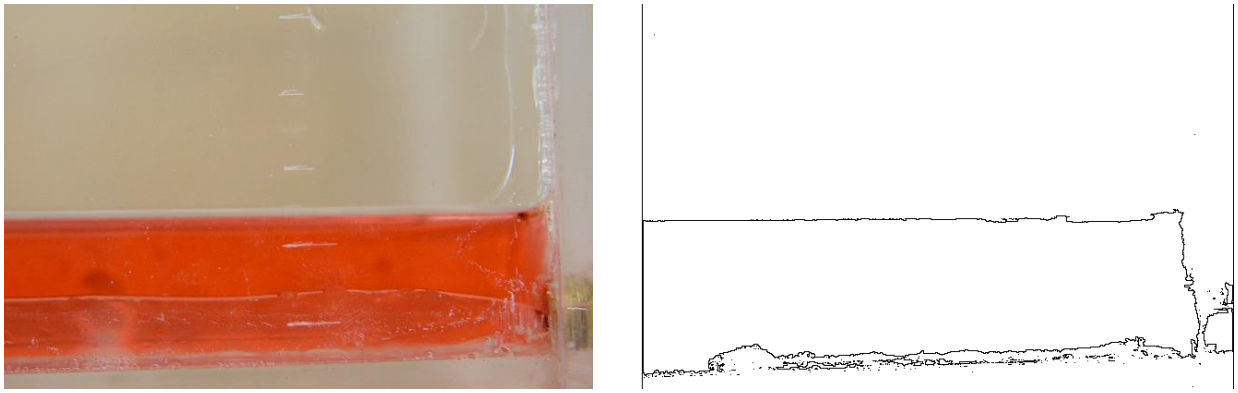

(a) (b)

Figure 22. (a) The red dyed kerosene dominates clear water in the image. (b) The image converted into 8-bit for image analysis.

A colorless kerosene and green cooking color for water was used to achieve maximum contrast as shown in Figure 23a. The red blue green (RBG) images were converted into the 8-bit images shown in Figure 23b where black area is water selected by ImageJ. Figure 23c shows the outline of water, which is the surface area of water in the image. The volume of water in the fuel tank is equal to the surface area of water times the 15 cm which is the breadth of the fuel tank.

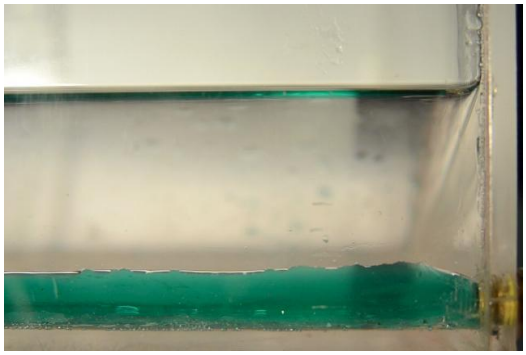

(a)

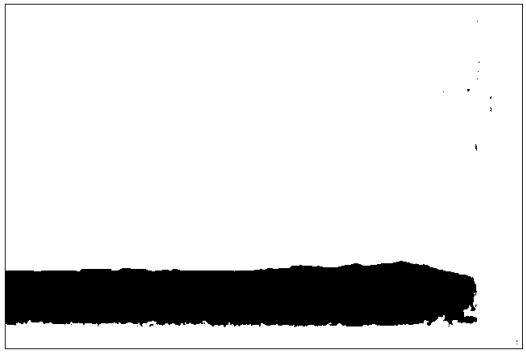

(b)

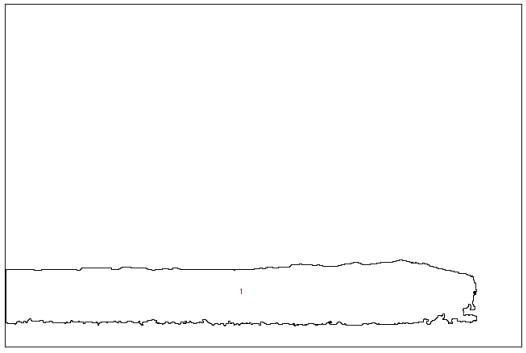

(c)

Figure 23. (a) Clear kerosene and green dyed water used for the experiments. (b) Converted the RBG image into 8-bit for analysis. (c) Outline of the 8-bit image after analysis.

3.3 Determination of the Tank Tilt Angle Relative to the Gravitational Vector

An aircraft in flight has constant velocity, zero pitch, and zero roll angle during cursing. There are usually two times when the aircraft is either pitch up or pitch down, when it is taking

off and when it is landing. Most small commuter aircrafts follow a similar pattern while taking off and landing. The flight pattern of an aircraft is provided in the owner manual of the aircraft, which is provided with the aircraft by the manufacture. Taking off and landing charts are used to determine the length of the runway required by the aircraft. These charts can also be used to determine the angle of the aircraft while ascending and descending. Figure 24 shows the time and the distance required, to achieve the desired altitude. The chart shows the time for a PA-28-181 to reach 12,000 feet is about 41 minutes.

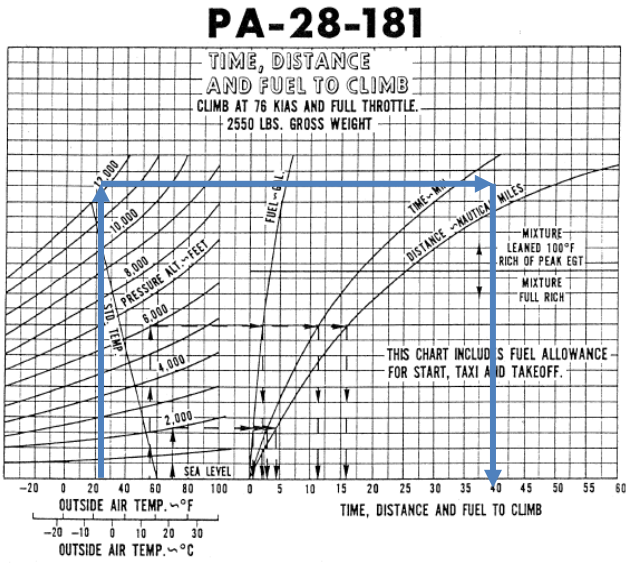

Figure 24. Climb chart for the PA-28-181.

From Figure 24 can be observed that the time required to achieve the desired altitude of 12,000 feet = 3657.6 meters is about 41 minutes, and the maximum takeoff speed is 85 MPH = 38 m/s. The Table *3* lists the parameters for determining the angle of incline for PA-28-181 aircraft. Using basic trigonometry the angle of climb can be found using Equation 3.1.

$$\theta = \sin^{-1}\frac{3657.6}{93480} = 2.24° \tag{3.1}$$

Table 3.

Parameters used to find the angle while taking off.

Description	Value
Maximum takeoff speed	85 mph = 38 m/s
Time to reach the desired height	41 minutes = 2460 seconds
Distance travelled during takeoff	38 m/s × 2460 seconds = 93,480 [m]

The angle of climb determined is 2.24º. The lift angle of the wing is 15º. The tank of the airplane is housed inside the wing. Adding in the lift angle of the wing and the angle of climb together equals the total angle of the tank while takeoff is 18.24º. Figure 25 shows the time and the distance required for the aircraft while landing. Figure 25 can also be used to determine maximum angle of the landing. The chart shows the time for a PA-28-181 to reach ground level form 12,000 feet is about 29 minutes. Table 4 shows the time and the distance required to reach ground level from 12,000 feet. Using Equation 3.1 the angle of landing is 9.4º + 15º = 24.4º.

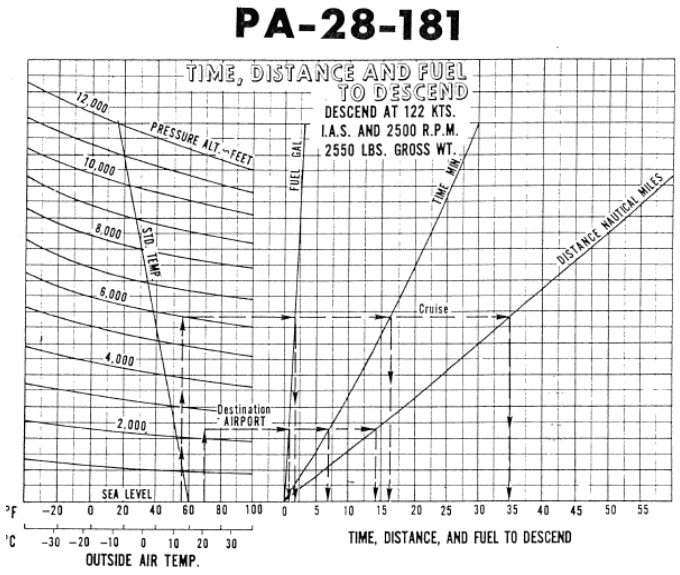

Figure 25. Descend chart for the PA-28-181.

Table 4.

Calculations for finding the angle of decent

Description	Value
Maximum takeoff speed	77 mph = 34.42 m/s
Time to reach the desired height	29 minutes = 1740 seconds
Distance travelled during takeoff	26,842.6 m

3.4 Calculation of Pressure Difference Due To the Pump

The Bernoulli Equation is used to calculate the pressure difference created by the fuel pump (Fox Robert, McDonald Alan, & Pritchard Philip, 2009). Equation 3.2 is the Bernoulli equation used in measuring the pressure difference.

$$\Delta P = P_1 - P_2 = \rho g \Delta z + \frac{1}{2}\rho f \frac{LV^2}{D} \tag{3.2}$$

f is the friction factor in Equation 3.2. Equation 3.3 is used to calculate the friction factor when the flow is in laminar regime.

$$f = \frac{64}{Re} \tag{3.3}$$

Re is the Reynolds number in Equation 3.3. The Reynolds number is defined in Equation 3.4

$$Re = \frac{\rho V D}{\mu} \tag{3.4}$$

where ρ is density, *V* is velocity, *D* is the diameter of pipe, and μ is the viscosity of liquid. Equation 3.5 is used for the fiction factor for the turbulent regime.

$$f = \left[1.14 - 2\log_{10}\left(\frac{e}{D} + \frac{21.25}{Re^{0.9}}\right)\right]^{-2} \tag{3.5}$$

e is the roughness coefficient, which depends on the material of the pipe, and *D* is the diameter of the pipe in Equation 3.5. The regime is determined by using the *Re* number. The flow is laminar if $Re < 2300$, and the flow is turbulent if $Re > 2300$. Table 5 shows the parameters used for calculating the pressure.

Table 5.

Parameters used in calculating pressure

Parameter	Nomenclature	Units	
		English	SI
Roughness	e	5e-6 [ft]	1.524e-6 [m]
Diameter	D	1/4 [inch]	6.35e-3 [m]
Flow rate	Q	2 [GPH]	2.103e-6 [m^3/s]
Water Density	ρ_{water}		1000 [kg/m^3]
Kerosene Density	$\rho_{kerosene}$		819 [kg/m3]
Water viscosity	μ_{water}		8.9e-4 Pa.s
Kerosene viscosity	$\mu_{kerosene}$		1.64e-3 Pa.s

The flow rate is converted into velocity by using Equation 3.6

$$V = \frac{Q}{A} \tag{3.6}$$

where Q is the flow rate and A is the area of the tube. Area is found by using Equation 3.7.

$$A = \pi \left(\frac{D}{2}\right)^2 \tag{3.7}$$

The velocity of the fluid is 6.64×10^{-2} m/s. Hence, the *Re* number for the kerosene using Equation 3.4 is 473.7, and the *Re* number for the water is 388.8. The flow is laminar flow since both values of Reynolds number is less than 2300. Plugging in the value of *Re* into the friction coefficient, the friction factor for the water is 0.135 and for kerosene is 0.165. The pressure for water is 3418.26 Pa, whereas the pressure for kerosene is 3561.24 Pa.

3.5 Calculation of G-Force Exerted On the Fuel Tank While Banking

Aircrafts experiences G-forces while banking (Cessna, 1978). The G-force is due to the centripetal force acting outward when the aircraft is in a turn (Bottega, 2006). Figure 26 illustrates the free body diagram of the aircraft when it is turning. In Figure 26, F_L is the lift force, F_N is the normal force, and the F_C is centripetal force.

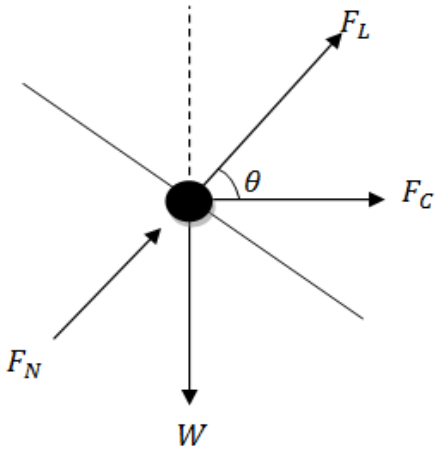

Figure 26. Free body diagram of an aircraft while banking.

Equation 3.8 is the centripetal acceleration, which states that

$$a = \frac{v^2}{r} \tag{3.8}$$

where *r* is the radius of the turn, and *v* is the velocity of the aircraft. Substituting Equation 3.8 into Newton's second law, $F = ma$, and replacing *F* with F_L or *L*, the equation yields to

$$L\ sin\theta = \frac{mv^2}{r} \tag{3.9}$$

where *L* is the lift of the aircraft, θ is the angle of banking, *m* is the mass of the aircraft, *v* is the velocity of the aircraft, and *r* is the radius of turn. In Equation 3.9, $L = mg$, where lift *L* at an angle θ is equal to the weight of the aircraft. Lift *L* yields to Equation 3.10 for an aircraft turning at an angle θ.

$$L = \frac{mg}{cos\theta} \tag{3.10}$$

Substituting the Equation 3.10 into Equation 3.9, this yields to Equation 3.11. Equation 3.11 is used to determine the G-force.

$$g = \frac{v^2}{r\ tan\theta} \tag{3.11}$$

Table 6 shows the information that is used to find the G force, obtained from the pilots manual (Cessna, 1978). Plug in the values from Table 6 into Equation 3.11 to determine the maximum allowable G-Force. Hence, the maximum allowable G's the PA-28-181 can tolerate is 3.78.

Table 6.

List of the values used in calculating the maximum G-Force.

Term	Value
Speed (v)	113 KIAS = 58.13 m/s
Approved banking angle	60º
Radius (r)	1690 ft = 515.1 m

3.6 Determination of Roll Frequency

An aircraft in roll motion, the weight of the aircraft is always pointing towards the earth (Stengel, 2005). The centripetal force is acting toward the center of the turning radius. The G-force is acting away from the circle. The lift is acting opposite of the weight. Figure 27 illustrates the free body diagram (FBD) of an aircraft in a roll.

From the FBD, Equation 3.12 shows the body forces acting in y-direction, and Equation 3.13 shows the body forces acting in x-direction.

$$F_{Lift}cos\theta = mg \tag{3.12}$$

$$F_{Lift}sin\theta + F_{certripetal} = m\ G_{Force} \tag{3.13}$$

Replacing $F_{Lift}sin\theta$ with $F_{Lift}\cos\theta\tan\theta$ in Equation 3.13 yields to Equation 3.14.

$$F_{Lift}cos\theta\ tan\theta + F_{centripetal} = \ m\ G_{Force} \tag{3.14}$$

Substituting $F_{Lift}\cos\theta$ from Equation 3.12 into Equation 3.14. $F_{centripetal} = \frac{mv^2}{r}$ is substituted into Equation 3.14 yields to Equation 3.15. Rearranging Equation 3.14 leads to Equation 3.15.

$$mg\ tan\theta\ + \frac{mv^2}{r} = G_{Force}m \tag{3.15}$$

$$v = \sqrt{r(G_{Force} - g\ tan\theta)} \tag{3.16}$$

Plugging the values of the distance of the fuel tank from the center of the fuselage, r = 2.5 m, the G_{force}, which is 3.78, and angle θ = 60º into Equation 3.16. The velocity of roll motion is 7.08 m/s. The time for the aircraft to roll from -60º to 60º is $T = 120\left(\frac{\pi}{180}\right)\left(\frac{2.5}{7.08}\right)$ = 0.738 seconds. The maximum frequency of the movement is $f = \frac{1}{0.738} = 1.35$ Hz. The value of the frequency is used in determining fluid's dynamic movement when the aircraft is in roll motion.

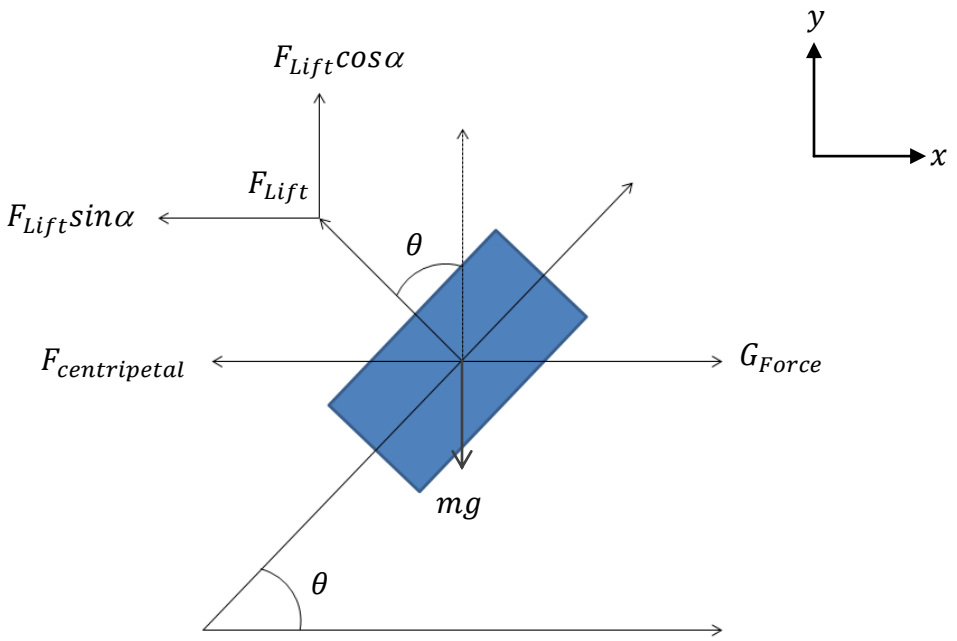

Figure 27. Free body diagram of an aircraft fuel tank in a roll.

3.7 Calculations for Liquid–Liquid Pressure and Velocity in Fuel Tank

Navier-Stokes Equation of momentum is used to determine the pressure and velocity. All the volume of fluids is behaving similarly in z-direction. Therefore, x and y axis are being studied (Zubkov, Serebryakov, Son, & Tarasova, 2005). Shown in Figure 28 is the FBD of two

immiscible liquids at an incline, where blue is water, red is kerosene, and θ is the angle of inclination.

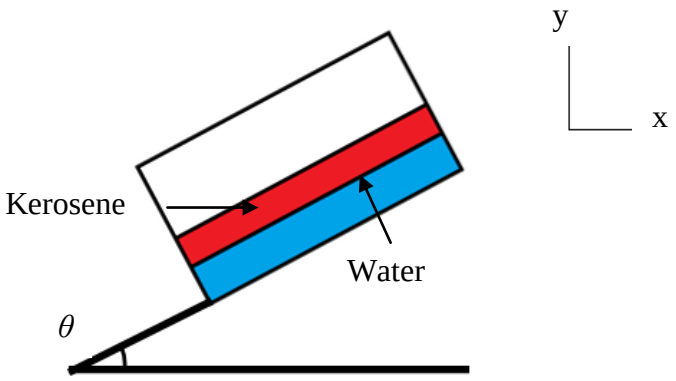

Figure 28. An illustration of fuel tank at an inclination having water and kerosene.

Equation 3.17 is used to determine pressure exerted by the pump on water, which is liquid 1. Equation 3.18 is the pressure exerted by the pump on kerosene, which is liquid 2.

$$P_1 = -\rho_1 g y + p_0 + g[\rho_1 h_1 + \rho_2 h_2] cos\theta + \Delta P_{pump} \quad (3.17)$$

$$P_2 = -\rho_2 g y + p_0 + g[\rho_1 h_1 + \rho_2 h_2]\, cos\theta + \Delta P_{pump} \quad (3.18)$$

The Boundary Conditions (BC) used for identifying the parameters affecting the velocity of water and kerosene are:

BC 1: No slip at the bottom of the tank $u_1(0) = 0$

BC 2: No viscous force on the free surface $\mu_2 = \frac{du_2}{dy}|_{y=h_1+h_2} = 0$

BC 3: Force balance at the fluid interface $\mu_1 \frac{du_1}{dy}|_{y=h_1} = \mu_2 \frac{du_2}{dy}|_{y=h_1}$

BC 4: Continuous velocity at the fluid interface $u_1|_{y=h_1} = u_2|_{y=h_1}$

Equation 3.19 shows the parameters affecting the velocity of water. Equation 3.20 shows the parameters affecting the velocity of kerosene.

$$u_1 = -\frac{gcos\theta}{2\upsilon_1}y^2 + \frac{gcos\theta}{\nu_2}(h_1 + h_2)y \tag{3.19}$$

$$u_2 = -\frac{gcos\theta}{2\upsilon_2}y^2 + \frac{gcos\theta}{\upsilon_2}(h_1 + h_2)y + g\left(\frac{h_1^2}{2} - (h_1 + h_2)h_1\right)\left(\frac{1}{\nu_2} - \frac{1}{\nu_1}\right) cos\theta \tag{3.20}$$

3.8 Setup of Computational Simulation

Laminar Two-Phase Flow Level Set Method interface was used to describe the fluid interface (Wilkes & Byke, 1999). COMSOL Multiphysiscs software was used to simulate the fluid dynamics in the tank. The dimensions of the fuel tank was setup in 2-D. The simulation was setup 32 cm W x 10.5 H cm, illustrated in Figure 29. The dimensions of the computer-simulated fuel tank were similar to the constructed fuel tank as previously shown in Figure 21. The walls were solid, therefore, at the boundaries no-slip condition (NS) was used, $u = v = 0$, where *u* is the velocity vector in the x-direction, and *v* is the velocity vector in the y-direction. Table 7 lists the physical parameters, domains, and colors associated with the liquids used in the simulation.

Table 7.

List of the physical parameters of the liquid used in the simulation.

Liquid	Domain	Color	Density [kg/m^3]	Dynamic Viscosity [Pa s]	Surface Tension [N/m]
Kerosene	1	Blue	819	1.64 e-3	0.087
Water	2	Red	1000	8.9 e -4	0.0728

The water's domain is 30 H cm x 1 cm H, which is $\frac{30}{336} \times 100 = 8.92\%$ of the kerosene's domain.

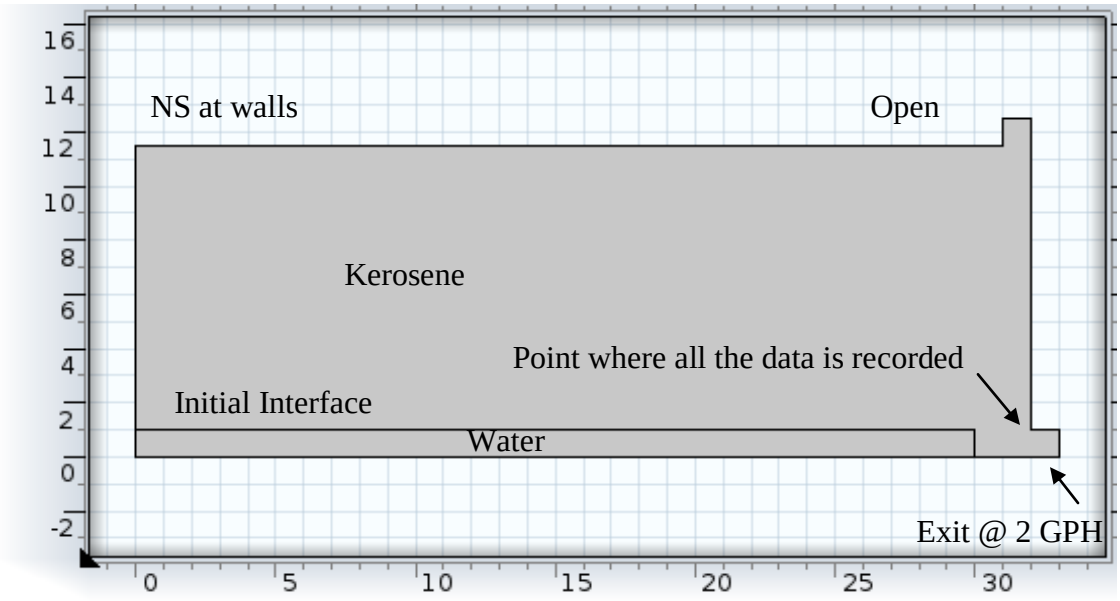

Figure 29. An experimental illustration of computer-simulated fuel tank.

3.8.1 Inlet and outlet conditions. Since the inlet of the aircraft is covered with a fuel cap and has an opening, thus for the inlet pressure $P_0 = 0$. The fuel pump creates a laminar flow of 2 GPH at the outlet. The outlet condition of the fuel tank was set at -2.106×10^{-6} m^3/s.

3.8.2 Body forces on the tank. Gravitational vector and G-force vector due to centripetal acceleration are acting as a body forces on the fuel tank during a roll. Both vectors change their direction due to the movement of the fuel tank. Equation 3.21 and Equation 3.22 show the gravitational vector and G-Force vector when an aircraft is turning left. Equation 3.23 and Equation 3.24 show the gravitational vector and G-Force vector when an aircraft is turning right.

$$g_x = -g\ F_G sin\theta \tag{3.21}$$

$$g_y = \ g\ cos\theta \tag{3.22}$$

$$g_x = g\ F_G sin\theta \tag{3.23}$$

$$g_y = -g\ F_G sin\theta \tag{3.24}$$

3.8.3 Sloshing of the fuel tank. When an aircraft is banking left and right or it is in a roll-motion, a sloshing effect may be occur in the fuel tank. The gravitational and G-Force become functions of movement frequency. Equation 3.25 and Equation 3.26 show the gravitational vector as a function of frequency in x and y directions, respectively.

$$g_x = g\ F_G sin\big(\theta\ sin(2\pi f t)\big) \tag{3.25}$$

$$g_y = g\ F_G cos\big(\theta\ sin(2\pi f t)\big) \tag{3.26}$$

Table 8 shows the values used for implementing the sloshing effect in the computer simulations.

Table 8.

Values of different constants for the gravitational vectors.

Denotations	Value	Explanation
g	9.81 [m/s^2]	Acceleration due to gravity
θ	60 [º]	Maximum banking angle while turning
F_G	3.8	G-force due to centripetal acceleration
f	1/10 [Hz]	Frequency at which the aircraft is banking

3.8.4 Initial and boundary conditions. As determined in Chapter 2, the tank of an aircraft is not pressurized, so the inlet of the tank in the simulations was set to be zero reference pressure. The volumetric flow rate at the outlet was set to be 2 GPH = 2.103×10^{-6} m^3/s. Table 9 lists the boundary conditions used.

Table 9.

List of boundary conditions used in the computer simulation.

Property	Values
Inlet pressure (P_O)	0
Outlet velocity	2 GPH = 2.031e-6 m^3/s
Walls	No slip

3.9 The Grid Independence Study

The oscillation experiment was performed on three different grid sizes to ensure that the solution is independent of the grid size (Sellier, Lee, Thompson, & Gaskell, 2009). Each

numerical experiment was simulated until 2.5 seconds to observe if the results are independent of the grid size. Figure 30(a, b, c, d) are the snap shots of the domain used for the grid independence study using 3063, 5060, 7716, and 10446 number of elements, respectively. Figure 31 shows the comparison of volume fraction of liquid at 2.5 seconds into the simulation. Figure 31(a, b, c, d) are the results of the simulations after 2.5 seconds using 3063, 5060, 7716, and 10446 number of elements, respectively. The mesh size has an effect on domain of water in kerosene as seen in Figure 30. The volume comparison shows that the average volume of kerosene is 342.36×15=5135.4 cm^3 and has a standard deviation of 3.09×15=46.35 cm^3. Table 10 shows the results of average volume of kerosene after 2.5 seconds into the simulation with respect to the number of elements. Table 10 also shows that at 7716 grid size, the kerosene volume is 340.9×15=5113.5 mm^3, and at 10446, the kerosene volume is 339.8×15=5097 mm^3. There is not much difference in the volume calculation of kerosene from 7716 and 10446 grid points. The computer-simulated experiments were performed by using 7716 grid points.

Table 10.

Volume covered by the kerosene with respect to the number of elements.

#	**Number of elements**	**Kerosene volume [mm^3]**
1	3063	346.8×15=5202.0
2	5060	342.0×15=5130.0
3	7716	340.9×15=5113.5
4	10446	339.8×15=5097.0

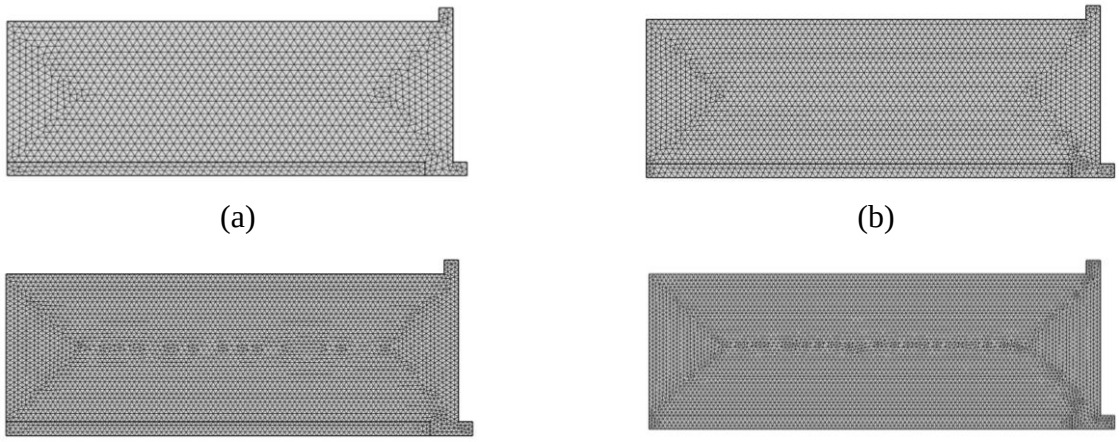

(a) (b)

(c) (d)

Figure 30. Snapshot of the elements used for grid independence study.

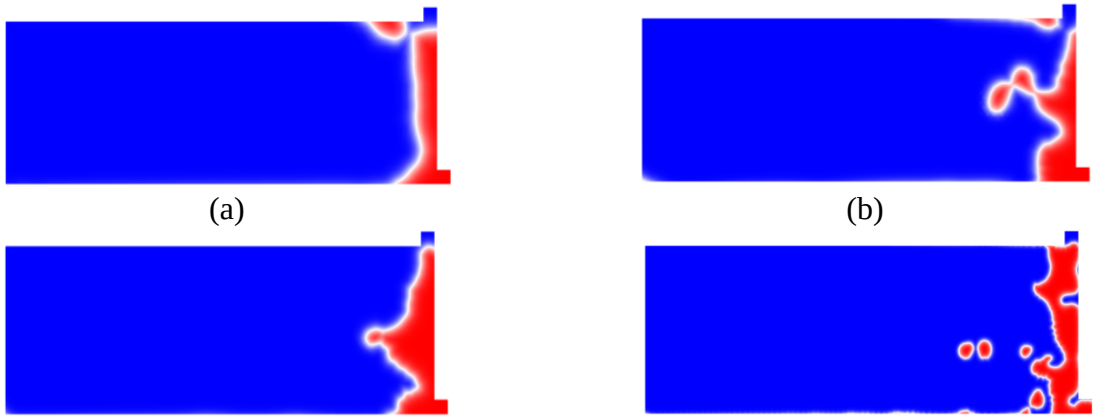

(a) (b)

(c) (d)

Figure 31. Comparison of simulations at time 2.5 seconds using different grid sizes.

3.10 Contact Angle and Interfacial Tension Measurements

Interfacial Tension and Contact angle are two important physical properties when determining the interfacial forces between fluids.

3.10.1 Surface tension. An interaction between a liquid and a gas or two immiscible liquids, the boundary between the phases are referred to as the fluid interface, also known as free surface. Surface tension is the force which is within the fluid interface (Iordan, 2000). The surface tension force exists because the cohesive forces holding the liquid molecules together are unbalanced due to the absence of liquid molecules on the gas side of the interface. The

intermolecular force within the liquid creates a net force towards the bulk of the liquid and the intermolecular forces of the free surface become stronger to maintain equilibrium to compensate for the imbalance. These strong intermolecular forces when between the molecules on the free surface are called surface tension; when there is an absence of gas, and there is another immiscible liquid, then this free surface is called interfacial tension (B.R.Munson, 2006).

To establish the relationship between the principal radii of the curvature of the free surface and the pressure difference across the free surface, consider the liquid drop as shown in Figure 32. The pressure difference across the free surface must be equal to force on the free surface due to surface tension in order for the liquid droplet to be in equilibrium. The first step toward creating equilibrium is to determine the pressure difference across the free surface.

$$F_P = (P_L - P_G)(\pi r^2) \tag{3.27}$$

In Equation 3.24, F_P is the net force due to the pressure difference across the free surface, P_L is the internal pressure of the liquid, P_G is the pressure of the surrounding gas, and πr^2 is the surface of the droplet resting on the solid surface where r is the radius of the droplet in contact with solid surface. The pressure of the surrounding gas, P_G, can be replaced with the pressure of the surrounding immiscible liquid, P_{SL}, leads to Equation 3.28

$$F_P = (P_L - P_{SL})(\pi r^2). \tag{3.28}$$

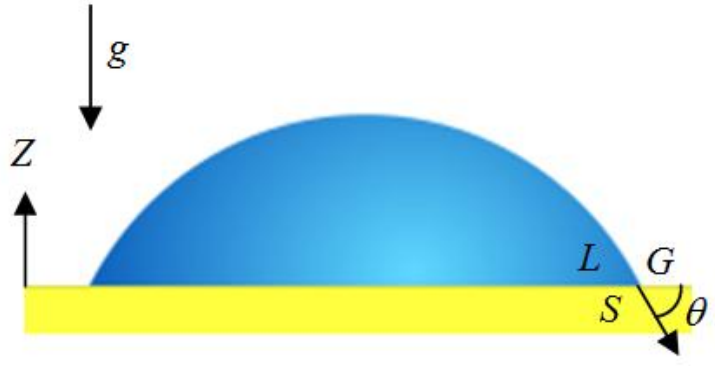

Figure 32. A two dimensional illustration of liquid drop on top of a solid surface.

To determine force F_P, consider the two dimensional representation of a droplet illustrated in Figure 33, where q is a point of interest along the curvature of the droplet, α is the angular position of q, R is the radius of the droplet, F_γ is the surface tension force, and F_z is the vertical component of the surface tension force. The vertical component of the force is due to surface tension as shown in Figure 33. F_z can be defined by Equation 3.29.

$$F_z = F_\gamma \sin(\alpha). \tag{3.29}$$

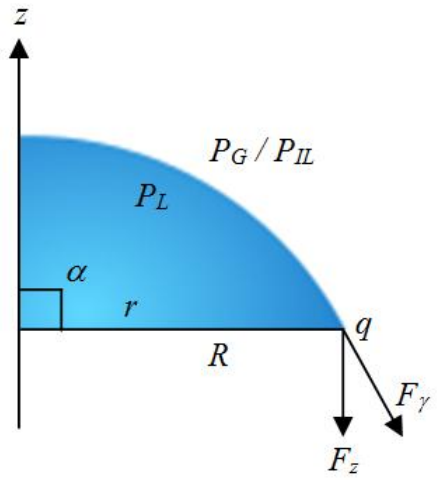

Figure 33. A free body diagram of the surface tension of the droplet

The vertical component of the force is due to the surface tension on the free surface. Force, F_z, is equally distributed along the circumference of the droplet. The total distributed force due to a surface tension on the free surface of the droplet, F_{total}, is defined in Equation 3.30.

$$F_{total} = F_\gamma \sin(\alpha)\,(2\pi r) \tag{3.30}$$

For the droplet to be in equilibrium, the pressure difference across the free surface and the distributed forced at surface tension must be equal. Equating Equation 3.28 and Equation 3.30 yields to surface tension force, F_γ, shown in Equation 3.31.

$$(P_L - P_{SL})(\pi r^2) = F_\gamma \sin(\alpha)\,(2\pi r) \tag{3.31}$$

Redefining the surface tension force, F_γ, as γ, and rearranging Equation 3.31 yields to Equation 3.32.

$$(P_L - P_{SL}) = \Delta P = \frac{\gamma \sin(\alpha)\,(2\pi r)}{\pi r^2} = \frac{2\gamma \sin(\alpha)}{r} \tag{3.32}$$

For simplifications, let $r = R$ and $\alpha = 90°$ the angle α is 90° because the contact angle is perpendicular to the substrate surface. Equation 3.32 reduces to Equation 3.33, which is called the Young-Laplace Equation, defined for a spherical interface.

$$\Delta P = \frac{2\gamma}{R} \tag{3.33}$$

Equation 3.29 is known as the Young-Laplace Equation if both principal radii are equal, $R = R_1 = R_2$. However, the principal radii are generally not equal when calculating surface tension, $R_1 \neq R_2$. Therefore, Equation 3.34 becomes

$$\Delta P = \gamma \left[\frac{1}{R_1} + \frac{1}{R_2}\right]. \tag{3.34}$$

In Equation 3.34, R_1 and R_2 are the principal radii of the droplet (m), γ is the surface tension (mN/m), and ΔP is the pressure difference between the liquids (N/m^2). Equation 3.34 is the called Young-Laplace Equation for droplets whose radii are not equal. Equation 3.34 will be used for the study the surface tension. Pendent drop method was used to determine the principal radii. R_1 and R_2 were measured by using image processor, ImageJ. Equation 3.35 is used to determine the pressure difference, ΔP.

$$\Delta P = \Delta \rho g h \tag{3.35}$$

In Equation 3.35, $\Delta\rho$ is the density difference in of the mediums (kg/m^3) and h is the length of the droplet (m).

3.10.2 Contact angle. The other relevant property of fluids is the contact angle. Contact angle of a liquid is defined as the angle at which the liquid meets a solid surface and is independent of gravity and the shape of the solid surface. The contact angle is determining the wettability of the liquid on a specific surface as explained in Chapter 2. The contact angle depends on the material the solid surface is made of and the fluid surrounding of liquid. The contact angle is the thermodynamic equilibrium between the three phases: the liquid (*L*) phase of the drop, the solid phase (*S*), which is the substrate, and the vapor phase (*V*). The vapor phase can be replaced with the liquid (*L*) if the droplet is surrounded by an immiscible liquid (Bernardin, et al., 1997). Equation 3.36 is used to find the contact angle and it is called Young's Equation

$$\gamma_{LV} cos\theta = \gamma_{SV} - \gamma_{SL} \tag{3.36}$$

where γ_{SL} is the Solid-Liquid surface tension, γ_{SV} is the Solid-Vapor surface tension, γ_{LV} is the Liquid-Vapor surface tension, and where as θ is the contact angle, as illustrated in Figure 34. Rearranging Equation 3.37, the contact angle, θ, can be calculated.

$$\theta = \cos^{-1}\left[\frac{\gamma_{SV} - \gamma_{SL}}{\gamma_{LV}}\right] \tag{3.37}$$

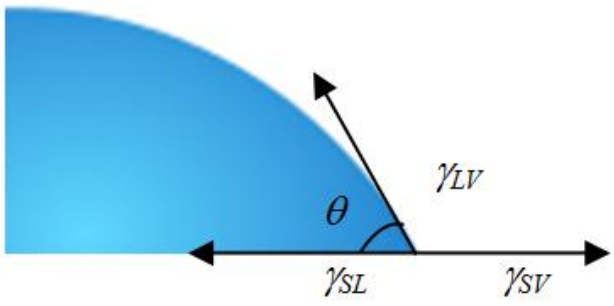

Figure 34. Force balance at three-component contact angle

3.10.3 Hardware assembly for interfacial tension measurement. The experimental setup used for measuring interfacial tension and the contact angle of water surrounded by kerosene are illustrated in Figure 35, where (1) is Backlights, (2) is Table, (3) is Syringe, (4) is Container, (5) is Shop vise, (6) is the Camera, and (7) is Tripod. Special attention was given to the cost and the ease of setup. All the parts used for the measurement of the contact angle and for measuring the interfacial tension are listed in Table 11.

Table 11.

List of components used in the experiment to measure the contact angle.

#	Brand	Specification	Quantity
1	Nikon	Camera, D5100 - 16.2 Mega Pixel	1
2	Nikon	Lens, Nikon 24 - 85 mm 1:2.8 - 41 Micro lens	1
3	Nikon	Lens, Nikon 40 mm 1:2.8 G Micro lens	1
5	Cowboy Studio	Lighting, 3300 Watt Softbox Video Lighting	1
4	Generic	Tripod	1
7	Generic	Diffuser paper/cloth	1
8	Generic	Holder shop vice	1

Description of Equipment: A Nikon D 5100, 16.2 megapixel, digital camera was used to take the shots. This camera was picked because of its capability of taking shots remotely (KING, 2011). The operator can focus, set the white balance, set the ISO speeds, and trigger the camera to take shots remotely with a Universal Serial Bus, USB, connected to a computer. The other reason this camera was picked was that the camera's optics were readily available. Different types of optics were used to take clear pictures of the droplet.

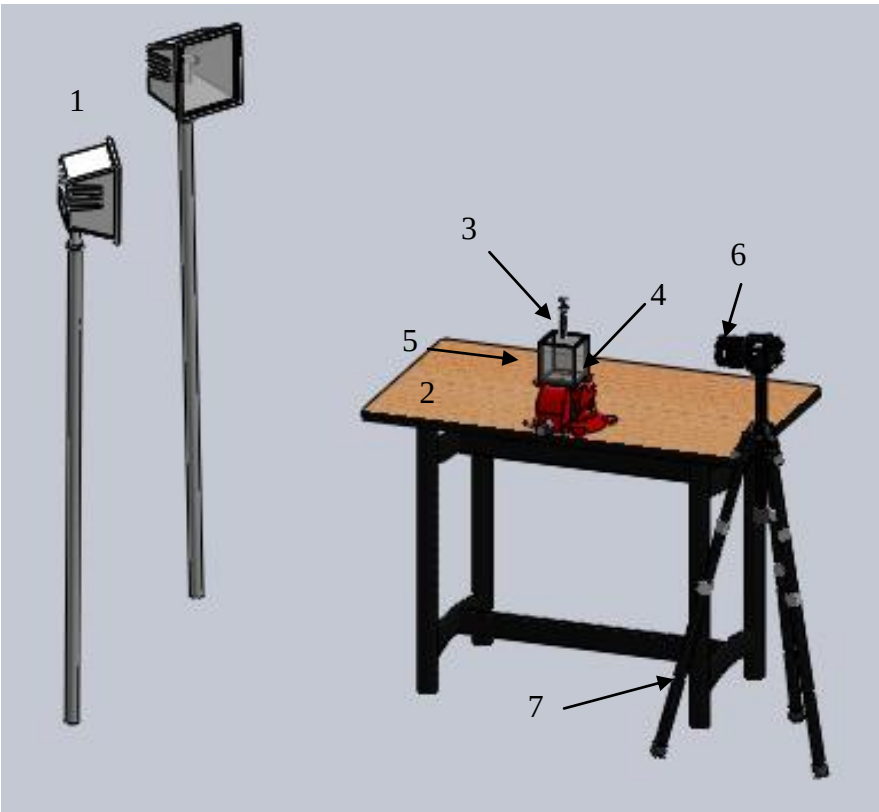

Figure 35. An illustration of the experimental setup to measure contact angle and interfacial tension of water droplet in various liquids.

The first lens used was the Nikon 24-85 mm 1:2.8-41 Micro lenses (Nikon, 2012b). There were two significant disadvantages using this lens. First, to observe the droplet, a combination of magnification lenses, +1, +2, and +4 were used to obtain a +7 magnification. Tiffen manufactured the magnification lenses (Sidhu & DeMetz, 1996). The magnification increased the droplet size in the frame, but the picture lost its sharpness. The other reason this lens was not used for later experiments, was that the lens did not have any autofocus or manual remote focusing ability. The focus of the camera had to be adjusted after changing the specimens. The scenario would result in disturbing the water droplet position, and sometimes the placement of the camera itself.

A new lens, the Nikon 40 mm 1:2.8 G Micro was used to achieve clear and close up shots (Nikon, 2012a). The lens has the ability to focus up to 40 mm, which was sufficient for our purposes. No magnification lenses were required with this lens, and the lens had the ability to autofocus and manual focus using remote software. The remote control software used was ControlMyNikon (Tetherscript, 2012). The remote software is discussed in image analyses part of this chapter.

A shop vise was used to hold the test subject. The shop vise was of a generic brand and mounted to the side of a worktable. The experimental setup was acceptable as long as the worktable does not move due to any external disturbance.

A generic brand of backlight manufactured by Cowboy Studio was used to achieve maximum contrast. The backlight had the ability to achieve maximum of 3300 Watts of soft light. The backlight was covered with a diffusion cloth for lighting to have equal distribution. The diffusion cloth can be used of differently colored depending on the color of the test subjects in order to achieve maximum contrast. Maximum contrast was extremely crucial for the analysis because the free surface of the droplet had to be clearly visible.

The experiment was covered to keep any stray light out. Any stray light would have disturbed the measurements since any light reflected off the droplet would temper with the profile of the droplet in the picture. The cover can be eliminated if the experiment is performed in a dark room.

A generic tripod was used to hold the camera. The tripod had the ability to move up and down, tilt -70 to 70º, and pan 360º. The movement of the tripod was essential to capture clear images.

A small container of 4 in W x 4 in H x 4 in D was constructed using acrylic plastic to measure the interfacial tension and contact angle of the water surrounded by kerosene. The sides of the container must be scratch free to ensure that the pictures of the droplets appear clear. Figure 36 illustrates the dimensions of the container used for measuring interfacial tension and contact angle.

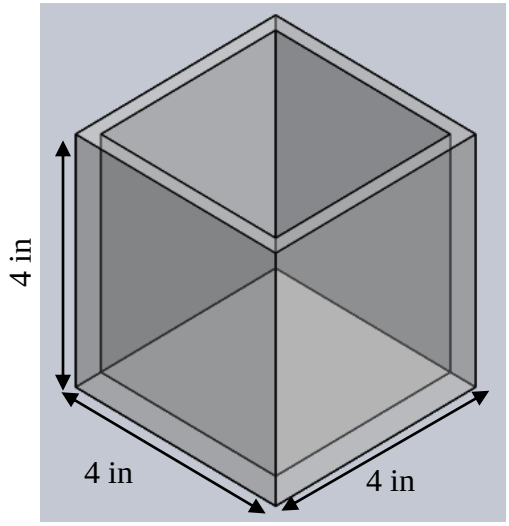

Figure 36. An illustration of the fabricated container.

3.11 Measuring Contact Angle and Interfacial Tension by Image Processing

The contact angle and the interfacial tension of water droplet were measured by placing water droplet of 10 micro liters on a substrate of acrylic and another 10 micro liters on aluminum substrate. Green food coloring was used to observe the water drop clearly in the picture. The droplets were placed using a 10 micro liter hypodermic needle, manufactured by Hamilton (Guide, 2006). As discussed earlier, a small acrylic container was fabricated for the experiments of immiscible liquid.

The camera was connected to the computer using a USB connection. A OEM software, ControlMyNikon v3.0.0.400, developed by Tetherscript Technology Corp (Tetherscript, 2012)., was used to control the camera. This software can control the camera's functions i.e. ISO

settings, white balance, the trigger to shoot the frame, and the focusing of the lens. The picture files were saved in jpeg format because jpeg are easily accessible by other software.

An open source software, ImageJ v1.44p, was used for image analysis (Abramoff, Magelhaes, & Ram, 2004). An angle finder tool was used to measure the contact angle (Whitfield, 2007). Figure 37a illustrates the droplets on the acrylic surface surrounded by air and Figure 37b on the acrylic surface surrounded by kerosene. An aluminum plate was placed in the acrylic container. Kerosene was filled in the container to measure the contact angle of water in kerosene. The side of the container had to be clear of any scratches. The pictures will not emerge clearly, if there were any scratches on the surface of the container. Figure 38 shows the measurement of the contact angle of a water droplet on aluminum substrate surrounded by air and a water droplet is surrounded by kerosene, respectively.

The images were converted into 8-bit, black and white, images in ImageJ software. Figure 39a is an 8-bit image of the contact angle of a water droplet on acrylic surrounded by air. Figure 39b is an 8-bit image of the contact angle of a water droplet on acrylic surrounded by kerosene. Figure 39c is an 8-bit image of the contact angle of a water droplet on aluminum surrounded by air. Figure 39d is an 8-bit image of the contact angle of a water droplet on aluminum surrounded by kerosene.

To measure the interfacial tension of the water droplets, the same open source software, ImageJ v1.44p, was used. Small movie clips were recorded in order to capture the precise moment the weight of the water droplet equaled to the surface tension force instead of taking photos. The movies were transferred into another open source software, VirtualDub v1.9.11 (Lee, 2001). Here, the video files were cropped and converted into image sequences. A reference length should be shown inside the picture frame to measure the radii of the droplets.

The diameter of the needle was used as a reference length whose diameter is 0.812 mm. The software was set to measurement of pixel versus length. A reference length in the frame makes the optical zoom of the camera irrelevant because there would be a reference length in the frame, which would also be zoomed in the frame as well (Abramoff, et al., 2004). Figure 40a illustrates the interfacial tension of water in the air and Figure 40b illustrates the interfacial tension of water in kerosene.

(a) (b)

Figure 37. (a) Contact angle of water droplet on acrylic surrounded by air. (b) Contact angle of water droplet on acrylic surrounded by kerosene.

(a) (b)

Figure 38. (a) Contact angle of water droplet on aluminum surrounded by air. (b) Contact angle of water droplet on aluminum surrounded by kerosene.

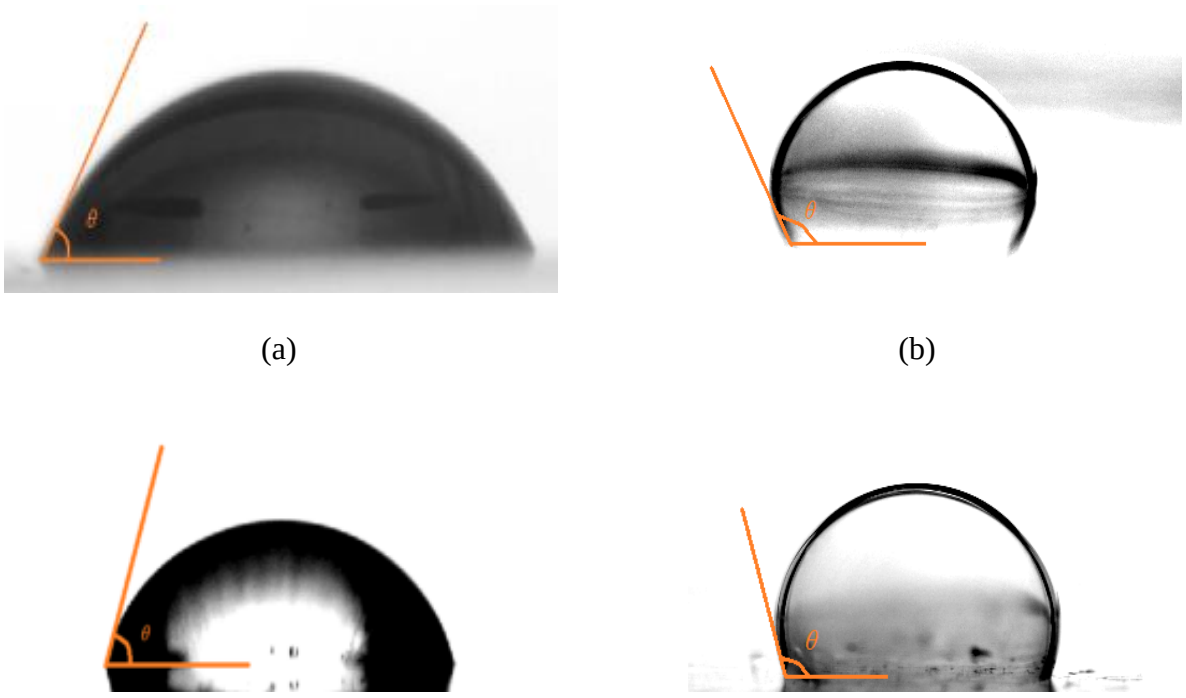

(a) (b)

(c) (d)

Figure 39. 8-bit images of water droplets for the measurement contact angles.

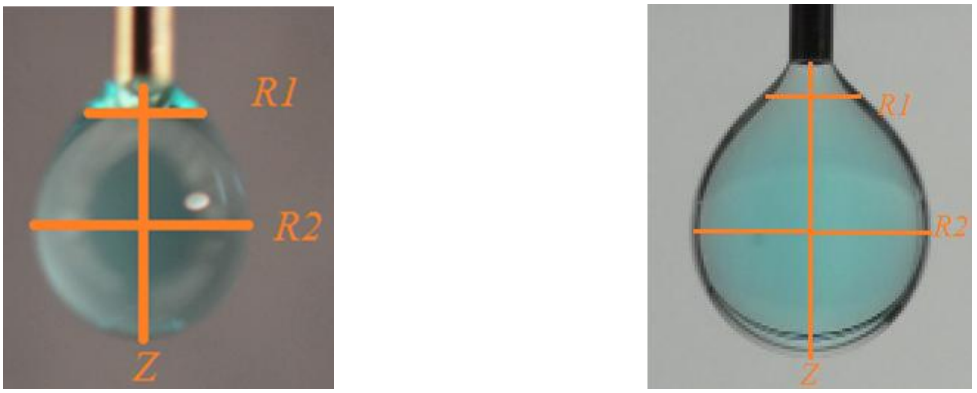

(a) (b)

Figure 40. (a) Measurement of the interfacial tension of water in air. (b) Measurement of the interfacial tension of water in kerosene.

R1 and *R2* are the principal radii of the droplet and *Z* is the height of the droplet in Figure 40. The values of principal radii and length are used in the Young's Equation, discussed earlier.

3.12 Experimental Uncertainties

Average values, and the standard deviation were found to determine the uncertainties in the experiment (Coleman & Steele, 2009). The experiments were repeated multiple times to have an average number using Equation 3.38. A standard deviation was determined for the experiment using Equation 3.39.

$$x_{AV} = \frac{1}{n}(x_1 + x_2 + x_3 + \cdots + x_n) \tag{3.38}$$

$$s_x = \sqrt{\frac{1}{n-1}[(x_1 - x_{AV})^2 + (x_2 - x_{AV})^2 + \cdots + (x_n - x_{AV})^2]} \tag{3.39}$$

In Equation 3.38, x_{AV} is the average value of the experiment, and n is the number of the trials. In Equation 3.39, s_x is the standard deviation.

CHAPTER 4

Results

4.1 Contact Angle and Interfacial Tension of Water and Kerosene

Table 12 lists the contact angles of water drop in the air and kerosene on aluminum and plexiglass. A water drop in kerosene is less wetting than one surrounded by air on the same surface. The average contact angle of water droplet, when surrounded by kerosene on aluminum, is 114.9º with a standard deviation of 13.97º. The average contact angle of water droplet, when surrounded by air on aluminum, is 49.6º with a standard deviation of 8.7º. Both experiments were repeated nine times. On the other hand, the average contact angle of water surrounded by kerosene is 121.1º with a standard deviation of 4.694º. The average contact angle of water surrounded by air is 64.6º with a standard deviation of 3.81º. The measurements of contact angle were repeated fifteen times to determine the statistical variation.

Table 12.

Contact angle measurements of water droplet in the air and kerosene.

	Kerosene	**Standard Deviation**	**Air**	**Standard Deviation**
Aluminum	114.9º	13.07º	49.6º	8.7º
Plexiglass	121.1º	4.7º	64.6º	3.81º

Table 13 lists the measurements of surface and interfacial tensions of water in the air and kerosene. The experiments were repeated three times and average data is reported. The average interfacial tension of the water droplet surrounded by air is 72.9 mN/m with the standard aviation of 3.68. The average interfacial tension is 6.78 mN/m with the standard deviation of 0.14. The measured results are necessary input for the numerical simulation experiment present later in the present Chapter.

Table 13.

Interfacial tension measurements of water droplet in various liquids.

	Air	Standard Deviation	Kerosene	Standard Deviation
Interfacial/Surface Tension	72.9	3.68	6.78	0.14

4.2 Experimental Simulation Results

The experimental setup and the procedure were presented in Chapter 3. The procedure required that 100 ml of water be added to 900 ml of kerosene to ensure that the consistency of the experiment was maintained. The following subsection present data under severe or limiting conditions found representative of normal aircraft operation.

4.2.1 Aircraft during taking-off and landing mode. Table 14 shows that average time required by water to clear the fuel line while the aircraft is in taking off or landing mode. The flying charts of the PA-28-181 were used to determine takeoff and landing angle of the aircraft. The takeoff and landing charts vary for different aircrafts. The maximum takeoff angle of a Piper Cherokee is 18.4º as explained earlier, and the maximum landing angle is 24.4º. The time required for 100 ml of water to move away from the entrance of the fuel line is 114.9 seconds while in takeoff mode and the time required while in landing mode is 121.8 seconds. The amount of water that remained in the tank measured from the side is 368.5×15=5527.5 mm^3=5.52 ml during takeoff mode while 391.5×5872.5 mm^3=5.87 ml remained during landing. The amount of water left in the fuel tank at takeoff inclination angle of the fuel tank is 5.52% of the original volume of water, whereas the amount of water left in the fuel tank left at landing inclination angle is the fuel tank is 5.87% of the original volume of the water.

Table 14.

Average residence time and volume of water in tank during taking off and landing

	Angle [deg.]	Average Time [sec.]	Average Volume [mm^3]	Average Volume [ml]
Taking off	18.4	114.9	368.5×15=5527.5	5.52
Landing	24.4	121.8	391.5×15=5872.5	5.87

4.2.2 Aircraft banking turns. Figure 41 shows the volume of water in the fuel tank versus the inclination angle of the fuel tank while the aircraft is in banking such that all the water accumulates at the exit port. Figure 41 shows that at 0º inclination, the volume of the water remaining in the tank is 573.47×15 = 8595 mm^3 = 8.59 ml The volume of water remaining in the tank is 222.83×15 = 3342.45 mm^3 = 3.34 ml at the tank inclination of 2.5º, which is a significant drop when compared to 0º tank inclination. Furthermore, when the tank inclination is 30º, the volume of water remaining in the tank reduces to 43×15 = 645 mm^3 = 0.64 ml, which is a more significant drop.

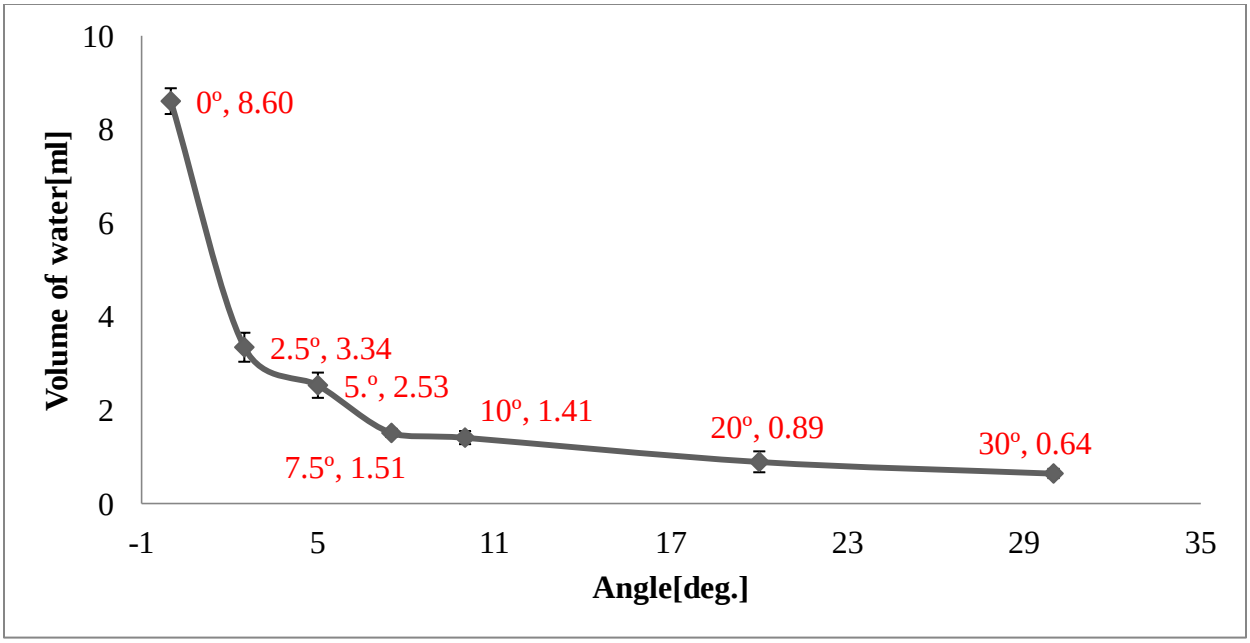

Figure 41. The water residue amounts in the fuel tank as a function of the tank inclination angle during aircraft banking mode.

Correspondingly, in Figure 42 the time required for water to clear the fuel line is plotted against inclination angle of the fuel tank. The Figure 42 shows the time required for the water to clear the fuel line port first deceases to a minimum before it increases as the tank inclination changes from 0 to 30º.

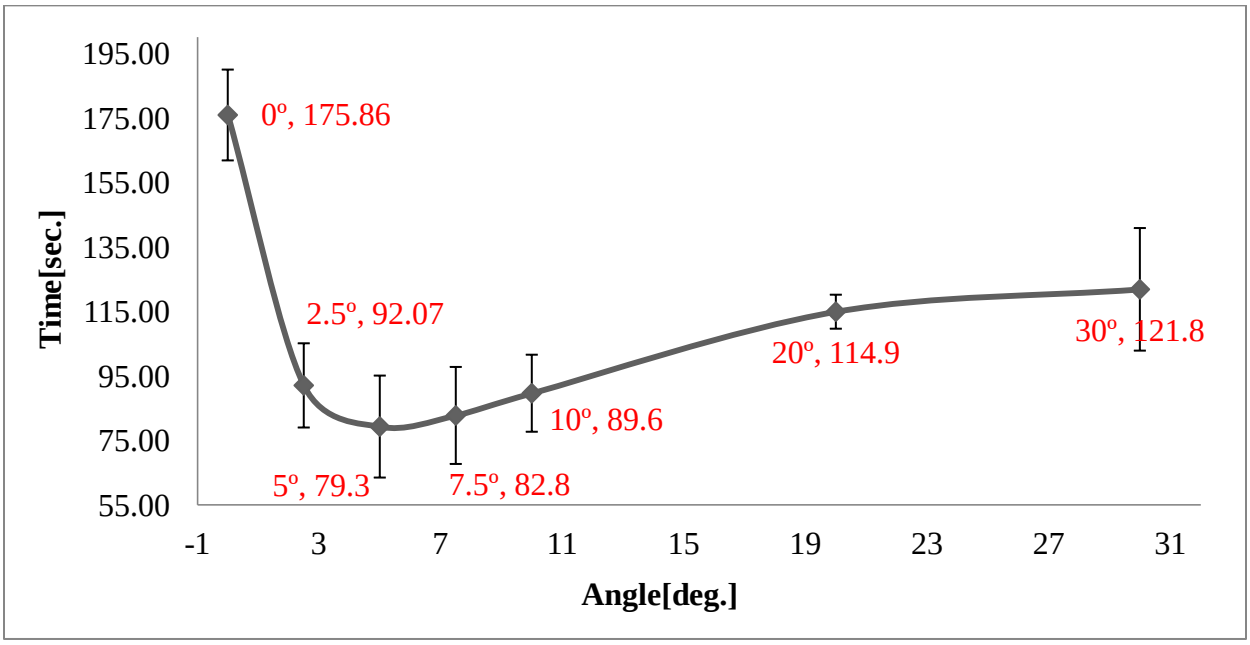

Figure 42. Time taken by water to clear the fuel line port area versus the fuel tank angle of inclination during banking.

To illustrate the water dispersion within the fuel tank, a series of aerial photographs were taken as shown in Figure 43. Figure 43a shows the water disperses into small pockets in fuel tank when the angle of tank inclination is small (less than 5º). On the other hand, when the angle of inclination is large (greater than 5º), the water has transforms into a continuous blob in the fuel tank as shown in Figure 43b. The aerial view of the tank shown in these figures explains the shape of graph in Figure 42, wherefore, at small tank inclination, water is dispersed into small pockets. On increase of the tank inclination, the small pockets of water agglomerate into a single blob hence, the volume of the water decreases as the angle of the fuel tank increases. Figure 44

shows the water contact line is pinned the bottom of the fuel tank. The pinning of water towards bottom of the water contact line at the bottom of the fuel tank determines the time when no water is entering the fuel line. Observing the change in the volume of water at the entrance of the fuel line gives another way to determine when on water exits fuel line. Change in the volume of water at the entrance means water is entering the fuel line. The water has moved away or pinned down at the entrance once the change in the volume of water discontinues. Water dispersion in small pockets for low inclination angle (less than 5º), and transformation of water into a continuous for high inclination angle (greater than 5º) blob explains the plot in Figure 41 where the volume of water at 0º is not equal to the initial volume of water. Since the water is in small pockets at low inclination angles, the water pockets are not in front of the viewing plane of the camera. While, the water transforms into a continuous blob, all the water moves in front of the viewing plane of the camera. The camera was set to show only water in front of the exit.

(a) (b)

Figure 43. (a) Top view of water (colored green) in dispersed in kerosene (less than 5º). (b) Top view of water (greater than 5º).

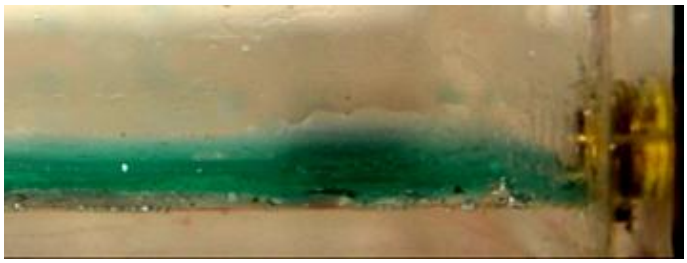

Figure 44. At the entrance of fuel line water domain pinning down towards the bottom of the fuel tank.

4.3 Simulation of Fuel-Water Dynamics in a Tank Subjected To External Forces

Discussed in Chapter 3, COMSOL Multiphysiscs software was used to simulate the right banking, the left banking, and the oscillation motions of the fuel tank in flight. Simulated experiments were picked because the test rigs inability to simulate the variable gravitational vector, and introduce the oscillation motions. In the following numerical simulation, the color red was chosen to water while the blue color was chosen to represent kerosene. The interface between the two phases was tracked by level set method as described in Chapter 3.

4.3.1 Simulation of fuel tank while aircraft is banking left. Figure 45 shows transient snap shots of water kerosene distribution at various times from initial state to the final state at 61 seconds after initiation. Figure 45a shows that at 0 second the water is at rest. Figure 45b shows that at 0.4 seconds the water is moving towards the right side of the tank. Figure 45c shows that at 6 seconds the water has stabilized perpendicular with respect to the direction of the gravitational vector. Figure 45d shows that at 61 seconds majority of water has left the fuel tank. The legend for the volume fraction is on the right side of Figure 45, where 1 is for water and 0 is for kerosene. The simulation experiment concludes that all the water moved towards the entrance of the fuel line with the introduction of a left turn.

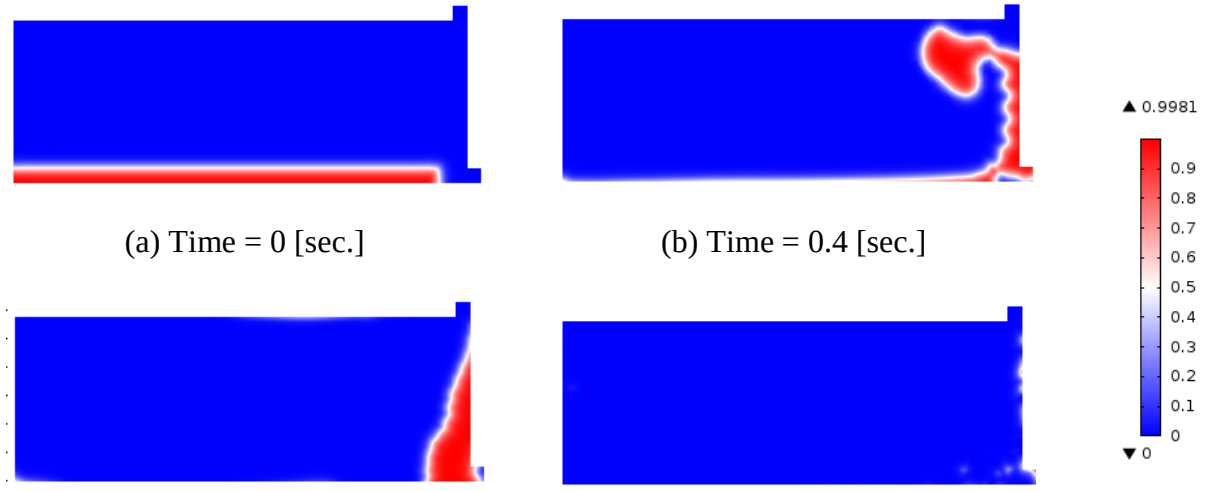

(a) Time = 0 [sec.]

(b) Time = 0.4 [sec.]

(c) Time = 6 [sec.]

(d) Time = 61 [sec.]

Figure 45. The dynamics of water due to gravitational forces caused by a left turn.

Figure 46 shows volume fraction of water at the entrance of the fuel line. The data was recorded at the entrance of the fuel line, shown in Figure 29. Figure 46 show that most of the water enters the fuel line before 30 seconds. From 31 seconds onwards, mostly kerosene is exiting the fuel tank. The spikes in Figure 46, from 31 seconds onward, suggests that water may enter the fuel line since some water may have transformed into small pockets due to disturbance in the gravitational vector.

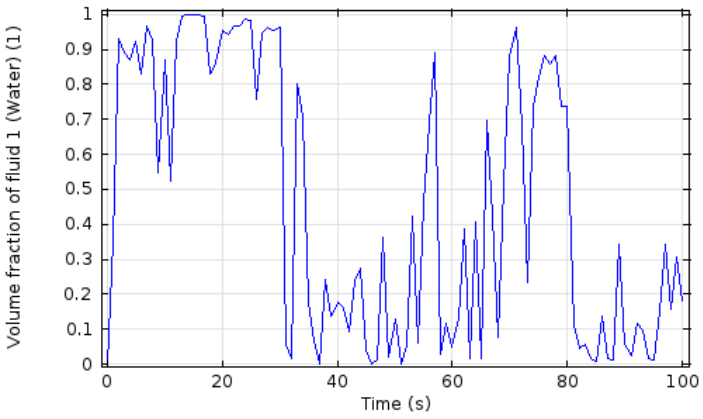

Figure 46. The volume fraction of water while turning left.

4.3.2 Simulation of fuel tank while aircraft is banking right. Figure 47 shows a snap shot of water kerosene distribution at various times from initial state to the final state at 5 seconds after initiation. After 5 seconds, the water remains in a stable phase and only kerosene is exiting the fuel tank. Figure 47a shows that at 0 second the water is at rest. Figure 47b shows that at 0.4 seconds water domain is moving towards the left side of the tank. Figure 47c shows that at 1.0 second the water domain is in motion, where top portion of water has broken into smaller pockets. Figure 47d shows that at 5 seconds the water domain has stabilized with respect to the direction of the gravitational vector. In the simulation experiment, when the right turn was introduced, all the water moved away from the entrance of the fuel tank.

Figure 48 is the plot for the volume fraction of water and kerosene. Mostly kerosene is exiting the fuel tank shown in Figure 48. The spikes shown in Figure 48 could be due to simulation error. This data was recorded at the entrance of the fuel line, shown in Figure 29.

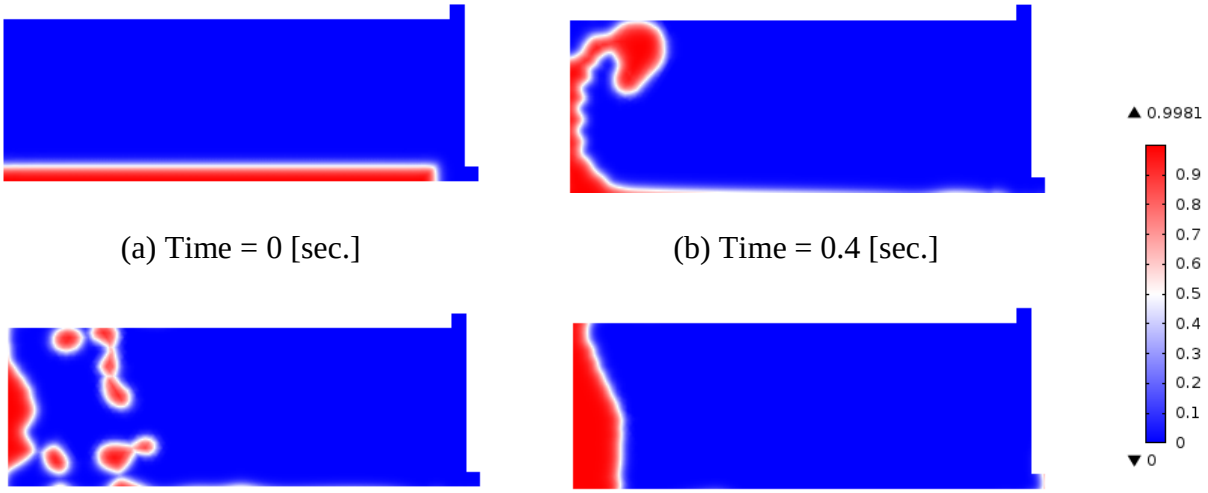

(a) Time = 0 [sec.] (b) Time = 0.4 [sec.]

(c) Time = 1.0 [sec.] (d) Time = 5 [sec.]

Figure 47. The dynamics of water due to gravitational forces caused by a right turn.

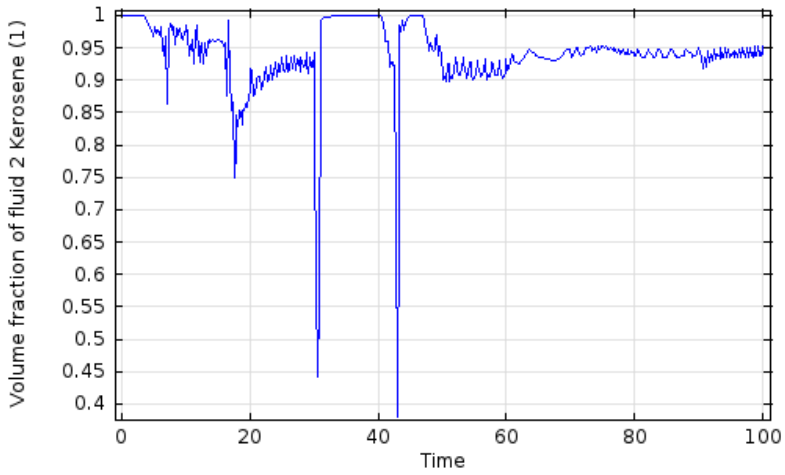

Figure 48. The volume fraction of kerosene while airplane turning right.

4.3.3 Fuel tank while in oscillation motion. In the computer-simulated experiment, an oscillatory motion was introduced to simulate the oscillation motion experienced by an aircraft. Figure 49a shows that at 0.1 second a ripple formation at the water and kerosene interface due to the introduction of the gravitational vector. Figure 49b shows that at 0.8 second the water domain is moving toward right due to the centripetal acceleration caused by the left turn motion. Figure 49c shows that at 19.6 seconds the water domain is moved to the left due to the centripetal acceleration caused by the right turn motion. Figure 49d shows that at 35.3 seconds most of the water is mixed with the kerosene.

The mixture of water and kerosene can also be observed in Figure 50. Figure 50 shows that the majority of the fluid entering the fuel line is water from 0 to 12 seconds. From 12 to 15 seconds only kerosene is entering. From 15 to 22 seconds again water is entering. Until 28 seconds the back and forth motion of water and kerosene continues. Both water and kerosene leave the fuel tank from 28 seconds onward. Figure 50 also concludes that from 28 seconds onward the water particulates have dispersed into kerosene. Data shown in Figure 50 was recorded at the entrance of the fuel line shown in Figure 29

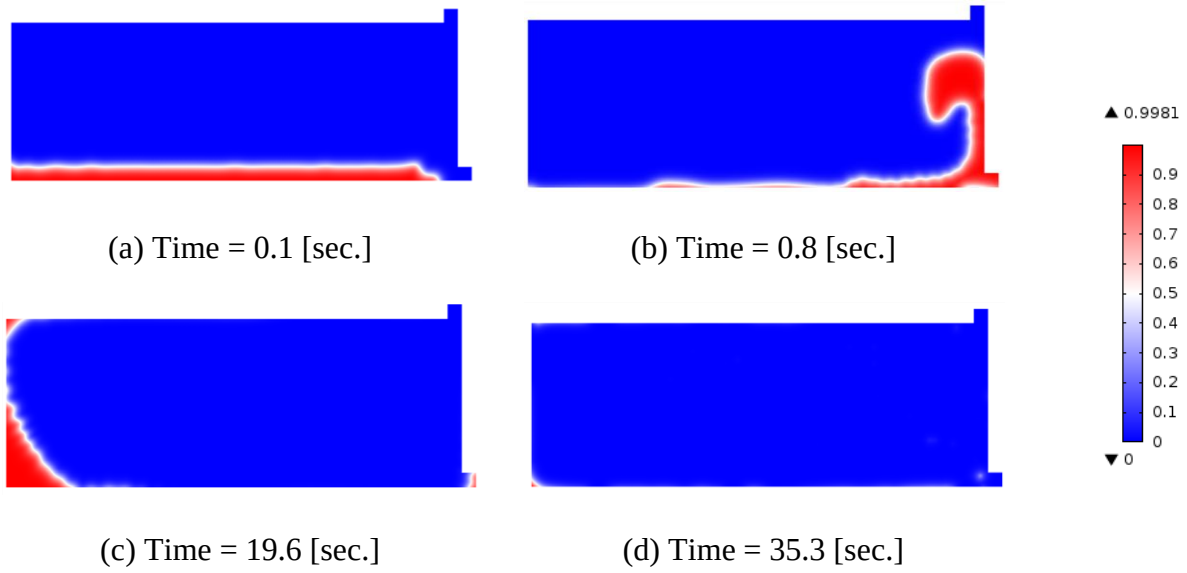

(a) Time = 0.1 [sec.] (b) Time = 0.8 [sec.]

(c) Time = 19.6 [sec.] (d) Time = 35.3 [sec.]

Figure 49. The dynamics of water caused oscillation motion of an airplane.

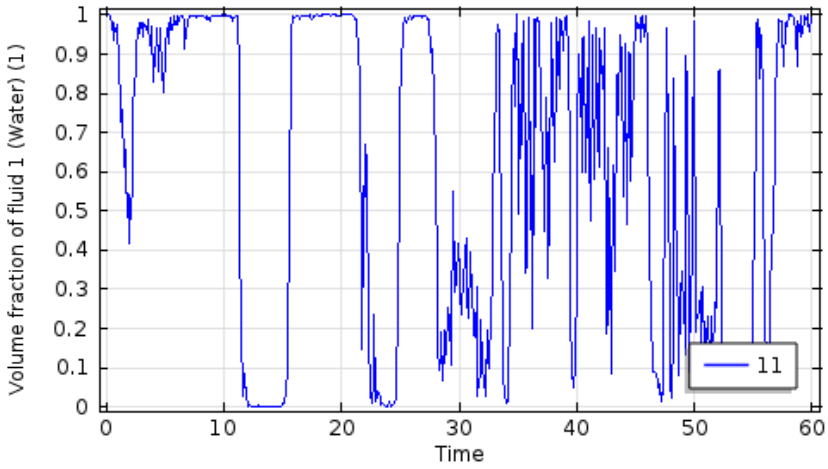

Figure 50. The volume fraction of kerosene during the airplane is in an oscillatory roll motion.

CHAPTER 5

Concluding Remarks and Future Research

The present study has considered various gravitational loading scenarios on the fuel tank that may influence the dynamics of the water therein and, thus, affect the probability of water entering the fuel line. Water in a fuel line may freeze to form ice, leading to the engine stalling. Whereas, the present research was not carried out at subzero temperatures, the scope was limited to dynamics of water above freeze to determine the probability of water presence in the fuel line. Specifically, the present thesis addressed the following two objectives: first is to measure interfacial properties of water in kerosene, in particular, surface tension or interfacial tension and contact angle. The second objective was to analyze the parameters that affect fuel-water dynamics in a fuel tank at varying tilt angles under simulated airplane maneuvers: (i) to determine the profile of water/kerosene interface, and (ii) to determine the time taken by water to clear the fuel-line exit port region under the same conditions.

All specific objectives were met. The results showed that the contact angle of water drop on plexiglass/Acrylic increases by 87.5% in kerosene compared to air. The contact angle of water drop on aluminum increases by 132% in kerosene compared to air. In addition, the interfacial tension between water and kerosene was measured as 6.78 mN/m, and the surface tension between air and water was confirmed to be 72.9 mN/m.

The second specific objective showed that the dynamics of water in a fuel tank are heavily influenced by the gravitational vector, magnitude, and frequency. The gravitational vector dictates whether the water enters the fuel line.

The gravitational loading scenarios concluded the following:

1. The airplane when banking left and right create centripetal acceleration. The centripetal acceleration interacts with gravity to create conditions that cause the water to move from the bottom of the tank to regions where the water will be ingested into the fuel line. These conditions are attributed to buoyancy driven convection.
2. Oscillatory motion of the fuel tank creates a complex water-distribution field, which leading to water entering the fuel line. The taking off and landing of the aircraft also affects the distribution of water in the fuel tank.

The study recommends that future research be performed to observe the dynamics of water and kerosene at subzero temperatures. The understanding the conditions, which promote phase change of water to ice in a highly dynamic situation, will lead to determining the conditions which deter ice formation in the fuel lines. The fuel flow to the engine will be uninterrupted as long as water does not form in the fuel line.

References

Abraham, F. F., & Zettlemoyer, A. (1974). Homogeneous nucleation theory. *Physics Today, 27*, 52.

Abramoff, M. D., Magelhaes, P. J., & Ram, S. J. (2004). Image processing with ImageJ. *Biophotonics Int, 11*(7), 36-42. doi: citeulike-article-id:2853779

Aldrich, E. W. (1931). Solubility of water in aviation gasolines. *Industrial & Engineering Chemistry Analytical Edition, 3*(4), 348-354.

Andrade, L., & Tenning, C. (1992). Design of Boeing 777 electric system. *Aerospace and Electronic Systems Magazine, IEEE, 7*(7), 4-11. doi: 10.1109/62.149784

Arashiro, E. Y., & Demarquette, N. R. (1999). Use of the pendant drop method to measure interfacial tension between molten polymers. *Materials Research, 2*(1), 23-32.

Ata, S., Pugh, R., & Jameson, G. (2011). The influence of interfacial ageing and temperature on the coalescence of oil droplets in water. *Colloids and Surfaces A: Physicochemical and Engineering Aspects, 374*(1), 96-101.

B.R.Munson, D. F. Y., T.H.Okiishi, and WW.Huebsch. (2006). Fundamentals Of mechanics. (6th).

Bernardin, J. D., Mudawar, I., Walsh, C. B., & Franses, E. I. (1997). Contact angle temperature dependence for water droplets on practical aluminum surfaces. *International Journal of Heat and Mass Transfer, 40*(5), 1017-1033. doi: 10.1016/0017-9310(96)00184-6

Black, C., Joris, G. G., & Taylor, H. S. (1948). The solubility of water in hydrocarbons. *The Journal of Chemical Physics, 16*, 537.

Bottega, W. J. (2006). *Engineering vibrations*: CRC Press.

Cao, Y., & Chen, K. (2010). Helicopter icing. *Aeronautical Journal, 114*(1152), 83-90.

Cessna. (1978). Pilot's Operation Handbook, 172N.

Christian, S. D., Slagle, A. R., Tucker, E. E., & Scamehorn, J. F. (1998). Inverted Vertical Pull Surface Tension Method. *Langmuir, 14*(11), 3126-3128. doi: 10.1021/la971384i

Coleman, H. W., & Steele, W. G. (2009). *Experimentation, validation, and uncertainty analysis for engineers*: John Wiley & Sons.

Croft, J. (2008). NTSB investigates Heathrow-like Trent 800 engine issue, from http://www.flightglobal.com/news/articles/ntsb-investigates-heathrow-like-trent-800-engine-issue-319956/

David, T., & Kin, M. (1999). Surface Tension Measurement *The Measurement, Instrumentation and Sensors Handbook on CD-ROM*: CRC Press.

Du, D. X., Geng, D. C., Sun, S. J., & Li, Y. G. (2012). Surface Tension Measurement by the Drop Volume Method. *Key Engineering Materials*, *501*, 407-412.

Du, Y. X., Gui, Y. W., Xiao, C. H., & Yi, X. A. (2010). Investigation on heat transfer characteristics of aircraft icing including runback water. *International Journal of Heat and Mass Transfer, 53*(19-20), 3702-3707. doi: DOI 10.1016/j.ijheatmasstransfer.2010.04.021

Dukhin, S. S., Kretzschmar, G., & Miller, R. (1995). *Dynamics of adsorption at liquid interfaces: theory, experiment, application* (Vol. 1): Elsevier Science.

Englin, B., Plate, A., Tugolukov, V., & Pryanishnikova, M. (1965). Solubility of water in individual hydrocarbons. *Chemistry and Technology of Fuels and Oils*, *1*(9), 722-726.

Fainerman, V., Miller, R., & Joos, P. (1994). The measurement of dynamic surface tension by the maximum bubble pressure method. *Colloid & Polymer Science*, *272*(6), 731-739.

Fortin, G., Mayer, C., & Perron, J. (2008). Icing wind tunnel study of a wind turbine blade deicing system. *Sea Technology, 49*(9), 41-44.

Fox Robert, W., McDonald Alan, T., & Pritchard Philip, J. (2009). Introduction to Fluid Mechanics: Hoboken, NJ: Wiley.

Guide, H. S. S. (2006). Syringe Selection.

Haines, L. (2008). Delta Boeing 777 engine suffers uncommanded rollback, *The Register*. Retrieved from http://www.theregister.co.uk/2008/12/10/delta_777_incident/

Hartland, S. (2004). *Surface and interfacial tension: measurement, theory, and applications* (Vol. 119): CRC Press.

Huttunen-Saarivirta, E., Kuokkala, V. T., Kokkonen, J., & Paajanen, H. (2009). Corrosion behaviour of aircraft coating systems in acetate- and formate-based de-icing chemicals. *Materials and Corrosion-Werkstoffe Und Korrosion, 60*(3), 173-191. doi: DOI 10.1002/maco.200805038

Institute, T. A. P. (2010). Kerosene/Jet Fuel Category assessment document. *US EPA*.

Iordan, K. (2000). Wetting or non-wetting liquid? *Physics Education, 35*(6), 435.

Isaac, G., Cober, S., Strapp, J., Korolev, A., Tremblay, A., & Marcotte, D. (2001). Recent Canadian research on aircraft in-flight icing. *Canadian Aeronautics and Space Journal, 47*(3), 213-221.

KING, J. A. (2011). Nikon d5100 for dummies (paperback). *Recherche, 67*, 02.

Lanicci, J., Halperin, D., Shappell, S., Hackworth, C., Holcomb, K., Bazargan, M., . . . Iden, R. (2012). General Aviation Weather Encounter Case Studies: FAA.

Lao, L., Ramshaw, C., Yeung, H., & Carpenter, M. (2011). Behaviour of Water in Jet Fuel in a Simulated Fuel Tank. *SAE Technical Paper*, 01-2794.

Lee, A. (2001). VirtualDub home page. *URL: www. virtualdub. org/index*.

Lewis, W. (1947). A flight investigation of the meteorological conditions conducive to the formation of ice on airplanes: National Aeronautics and Space Administration Moffett Field CA Ames Research Center.

Lunkenheimer, K., & Wantke, K. D. (1978). On the applicability of the du Nouy (ring) tensiometer method for the determination of surface tensions of surfactant solutions. *Journal of Colloid and Interface Science, 66*(3), 579-581. doi: 10.1016/0021-9797(78)90079-6

MacDonald, D. (2011). *Owner Assisted Aircraft Maintenance*: Alpha Zulu LLC.

Mittal, K. L. (2009). *Contact angle, wettability and adhesion* (Vol. 6): Brill Academic Publishers.

Murray, B., Broadley, S., Wilson, T., Atkinson, J., & Wills, R. (2011). Heterogeneous freezing of water droplets containing kaolinite particles. *Atmos. Chem. Phys, 11*, 4191-4207.

Murray, B. J., & Bertram, A. K. (2005). Formation and stability of cubic ice in water droplets. *Phys. Chem. Chem. Phys., 8*(1), 186-192.

Murray, B. J., Broadley, S. L., & Morris, G. J. (2011). Supercooling of water droplets in jet aviation fuel. *Fuel, 90*(1), 433-435. doi: http://dx.doi.org/10.1016/j.fuel.2010.08.018

Myers, T., & Hammond, D. (1999). Ice and water film growth from incoming supercooled droplets. *International Journal of Heat and Mass Transfer, 42*(12), 2233-2242.

Naterer, G. F. (2011). Multiphase transport processes of droplet impact and ice accretion on surfaces. *Cold Regions Science and Technology, 65*(1), 5-12. doi: 10.1016/j.coldregions.2009.09.005

Nevins, R. G., Rohles, F. H., Springer, W., & Feyerherm, A. (1966). A temperature humidity chart for thermal comfort of seated persons. *ASHRAE transactions, 72*(1), 283-291.

Nikon. (2012a). AF-S DX Micro-NIKKOR40mm f/2.8G

Nikon. (2012b). AF Zoom-Nikkor 24-85mm f/2.8-4D IF.

NOAA. (2001). Wind Chill Chart.

Noüy, P. L. d. (1925). An interfacial tensometer for universal use *Laboratories of The Rockefeller Institute for Medical Research*.

Padday, J. F., Pitt, A. R., & Pashley, R. M. (1975). Menisci at a free liquid surface: surface tension from the maximum pull on a rod. *Journal of the Chemical Society, Faraday Transactions 1: Physical Chemistry in Condensed Phases, 71*, 1919-1931.

Ratvasky, T. P., Barnhart, B. P., & Lee, S. (2010). Current Methods Modeling and Simulating Icing Effects on Aircraft Performance, Stability, Control. *Journal of Aircraft, 47*(1), 201-211. doi: Doi 10.2514/1.44650

Rensing, P. J., Liberatore, M. W., Sum, A. K., Koh, C. A., & Dendy Sloan, E. (2011). Viscosity and yield stresses of ice slurries formed in water-in-oil emulsions. *Journal of Non-Newtonian Fluid Mechanics, 166*(14), 859-866.

Rutherford, R. B. (2001). De-ice and anti-ice system and method for aircraft surfaces: Google Patents.

Saad, S. M. I., Policova, Z., & Neumann, A. W. (2011). Design and accuracy of pendant drop methods for surface tension measurement. *Colloids and Surfaces A: Physicochemical and Engineering Aspects, 384*(1–3), 442-452. doi: 10.1016/j.colsurfa.2011.05.002

Schramm, L. L. (2000). *Surfactants: fundamentals and applications in the petroleum industry*: Cambridge University Press.

Sellier, M., Lee, Y., Thompson, H., & Gaskell, P. (2009). Thin film flow on surfaces containing arbitrary occlusions. *Computers & Fluids, 38*(1), 171-182.

Sheng-Shan, Z. G. J. B. I., & Xin, W. U. J. T. L. I. (2011). A New Surface Tension Measurement System Based on Capillary Rise Method [J]. *Journal of Engineering Thermophysics, 4*.

Shitzer, A., & De Dear, R. (2006). Inconsistencies in the "New" Windchill Chart at Low Wind Speeds. *Journal of Applied Meteorology and Climatology, 45*(5), 787-790.

Sidhu, N., & DeMetz, C. (1996). Simulation of irregularly shaped electron treatment fields using a digital camera. *Medical Dosimetry, 21*(3), 159-163.

Stengel, R. F. (2005). Flight dynamics. *Aircraft Engineering and Aerospace Technology, 77*(3).

Taborek, P. (1985). Nucleation in emulsified supercooled water. *Physical Review B, 32*(9), 5902-5906.

Tetherscript, T. C. (2012). Control My Nikon.

Tulapurkara, E., Ananth, S., & Kulkarni, T. M. (2007). Performance Analysis of a piston engined airplane-Piper Cherokee PA-28-180.

U.K., A. A. I. B. A.-. (2010). Final Report on BA 777 Crash at Heathrow. *Aviation Today's Daily Brief, 2*(34), n/a.

Vali, G. (1971). Quantitative Evaluation of Experimental Results an the Heterogeneous Freezing Nucleation of Supercooled Liquids. *Journal of Atmospheric Sciences, 28*, 402-409.

Vargaftik, N., Volkov, B., & Voljak, L. (1983). *International tables of the surface tension of water*: American Chemical Society and the American Institute of Physics for the National Bureau of Standards Washington, DC.

Viades-Trejo, J., & Gracia-Fadrique, J. (2007). Spinning drop method: From Young–Laplace to Vonnegut. *Colloids and Surfaces A: Physicochemical and Engineering Aspects, 302*(1–3), 549-552. doi: http://dx.doi.org/10.1016/j.colsurfa.2007.03.033

Vonnegut, B. (1942). Rotating bubble method for the determination of surface and interfacial tensions. *Review of Scientific Instruments, 13*(1), 6-9.

Whitfield, E. (2007). Understanding the Physics Behind Recorded Motion.

Wilkes, J. O., & Byke, S. G. (1999). *Fluid mechanics for chemical engineers*.

Winter, A. (2010). 1/2010 G-YMMM.

Wood, G., & Walton, A. (1970). Homogeneous nucleation kinetics of ice from water. *Journal of Applied Physics, 41*(7), 3027-3036.

Xu, W. (2005). *Experimental Investigation of Dynamic Interfacial Interactions at Reservoir Conditions.* Louisiana State University.

Yanxia, D., Yewei, G., Chunhua, X., & Xian, Y. (2010). Investigation on heat transfer characteristics of aircraft icing including runback water. *International Journal of Heat and Mass Transfer, 53*(19-20), 3702-3707. doi: 10.1016/j.ijheatmasstransfer.2010.04.021

Zubkov, P., Serebryakov, V., Son, E., & Tarasova, E. (2005). Steady-state flow of two viscous immiscible incompressible fluids in a plane channel. *High Temperature, 43*(5), 769-774.